

High-Resolution Neural Network Demonstrates Strong CO₂ Source-Sink Juxtaposition in the Coastal Zone

**Key Points:**

- The coastal Northeast Pacific is a net sink for atmospheric CO₂ with increasing air-sea pCO₂ disequilibrium trends in most of the region
- Regional processes drive net annual air-sea CO₂ flux to be anticorrelated with air-sea CO₂ flux seasonal amplitude
- Estimated pCO₂ reproduces observed seasonal cycle phase and amplitude well along with broad spatial patterns of variability

Supporting Information:

Supporting Information may be found in the online version of this article.

Correspondence to:

P. J. Duke,
pjduke@ucalgary.ca

Citation:







Duke, P. J., Hamme, R. C., Ianson, D., Landschützer, P., Swart, N. C., & Covert, P. A. (2024). High-resolution neural network demonstrates strong CO₂ source-sink juxtaposition in the coastal zone. *Journal of Geophysical Research: Oceans*, 129, e2024JC021134. <https://doi.org/10.1029/2024JC021134>

Received 19 MAR 2024

Accepted 3 JUL 2024

Author Contributions:

Conceptualization: P. J. Duke, R. C. Hamme, D. Ianson, P. Landschützer, N. C. Swart
Data curation: P. J. Duke, P. A. Covert
Formal analysis: P. J. Duke
Funding acquisition: P. J. Duke, R. C. Hamme, D. Ianson
Investigation: P. J. Duke
Methodology: P. J. Duke, P. Landschützer
Project administration: R. C. Hamme, D. Ianson
Supervision: R. C. Hamme, D. Ianson
Visualization: P. J. Duke
Writing – original draft: P. J. Duke

P. J. Duke¹ , R. C. Hamme¹ , D. Ianson^{1,2} , P. Landschützer³ , N. C. Swart^{1,4} , and P. A. Covert² 

¹School of Earth and Ocean Sciences, University of Victoria, Victoria, BC, Canada, ²Institute of Ocean Sciences, Fisheries and Oceans Canada, Sidney, BC, Canada, ³Flanders Marine Institute (VLIZ), Ostend, Belgium, ⁴Canadian Centre for Climate Modelling and Analysis, Environment and Climate Change Canada, Victoria, BC, Canada

Abstract The role of coastal oceans in regulating atmospheric carbon dioxide remains poorly quantified and understood. Here, we use a two-step neural network approach to generate estimates from sparse observational data in the coastal Northeast Pacific Ocean at an unprecedented spatial resolution of 1/12° with coverage in the nearshore (0–25 km offshore). We compiled partial pressure of carbon dioxide (pCO₂) observations as well as a range of predictor variables including satellite-based and physical oceanographic reanalysis products. With the predictor variables representing processes affecting pCO₂, we created non-linear relationships to interpolate observations from 1998 to 2019. Compared to in situ shipboard and mooring observations, our coastal pCO₂ product captures broad spatial patterns and seasonal cycle variability well. A sensitivity analysis identifies that the parameters responsible for the neural network's ability to capture regional pCO₂ variability are associated with mechanistic processes, including mixed layer deepening, mesoscale eddies, and gyre upwelling. Using wind speed and atmospheric CO₂, we calculated air-sea CO₂ fluxes. We report an anticorrelation between annual air-sea CO₂ flux and its seasonal amplitude with the relationship driven by circulation, opposing seasonal upwelling/relaxation versus downwelling, and the effects of winter mixing and primary productivity. We show that the inclusion of nearshore net outgassing fluxes lowers the overall regional net flux. Overall, our results suggest that the region is a net sink (−0.7 mol m^{−2} yr^{−1}) for atmospheric CO₂ with trends indicating increasing oceanic uptake due to strong connectivity to subsurface waters.

Plain Language Summary The importance of the coastal ocean as a hub of exchange for carbon between terrestrial ecosystems, the open ocean, and the atmosphere is still unclear. In this study, we investigate how much carbon dioxide moves between the ocean and the atmosphere in the coastal Northeast Pacific. We use a mathematical technique (i.e., machine learning) to transform limited observational data to a high-resolution estimate of this exchange across the entire region. We found this method effectively captured the big picture patterns and seasonal changes in ocean carbon dioxide levels. We report that the coastal Northeast Pacific absorbs slightly more carbon dioxide than it releases, helping regulate atmospheric levels of this greenhouse gas. However, there are large differences regionally with some coastal zones absorbing substantial amounts of carbon dioxide and others releasing the gas, such as the nearshore. We report a trend of increasing ocean uptake over time, suggesting the region may play an increasingly important role in reducing atmospheric carbon dioxide levels. This study provides valuable baseline information for efforts to reduce carbon dioxide in the atmosphere through artificially enhancing ocean uptake in the region.

1. Introduction

The global ocean takes up nearly a quarter of anthropogenic carbon dioxide (CO₂) emissions annually (Friedlingstein et al., 2023). It has been suggested that coastal oceans contribute disproportionately to oceanic CO₂ uptake relative to the global ocean by surface area (Bourgeois et al., 2016; Chau et al., 2022; Laruelle et al., 2014; Resplandy et al., 2024; Roobaert et al., 2019, 2024), but exhibit far greater heterogeneity in air-sea CO₂ fluxes (Liu et al., 2010) and may be changing at a different rate compared to the open ocean (Laruelle et al., 2018; Resplandy et al., 2024). Coastal oceans serve as an important hub of exchange, outgassing carbon delivered by terrestrial ecosystems to the ocean (Regnier et al., 2022), while facilitating transport between the coast and open ocean, and directly absorbing CO₂ from the atmosphere (Bauer et al., 2013; C. Chen & Borges, 2009; Mackenzie et al., 1998; Ward et al., 2020). However, the role of the coastal ocean in the global carbon budget is not well-

© 2024. The Author(s).

This is an open access article under the terms of the [Creative Commons Attribution License](https://creativecommons.org/licenses/by/4.0/), which permits use, distribution and reproduction in any medium, provided the original work is properly cited.

Writing – review & editing: P. J. Duke, R. C. Hamme, D. Ianson, P. Landschützer, N. C. Swart, P. A. Covert

constrained due to lack of observations relative to the complexity of highly localized variability (Chavez et al., 2007; Dai et al., 2021, 2022).

Gap filling approaches (i.e., methods to interpolate sparse observations) used to inform coastal ocean air-sea CO₂ flux estimates are often at coarse resolution and methods of construction are potentially opaque to many users. Interpolation techniques have been widely used to inform air-sea CO₂ flux estimates in the coastal ocean both regionally and globally (e.g., S. Chen et al., 2016; Hales et al., 2012; Laruelle et al., 2017; Parard et al., 2015, 2016; Roobaert et al., 2019, 2024; Sharp et al., 2022; Xu et al., 2019). These approaches extend the temporal and spatial coverage of partial pressure of CO₂ in seawater (*p*CO₂) observations from community synthesis efforts (e.g., through the Surface Ocean CO₂ Atlas (SOCAT); Bakker et al., 2016) into regions where no observations exist, and can be used to calculate integrated air-sea CO₂ fluxes using wind speed and atmospheric CO₂ (Wanninkhof, 2014). Historically, coastal ocean approaches have been adopted from their open ocean counterparts (Chau et al., 2022; Landschützer et al., 2020), and thus most of these estimates have at best a monthly, 1/4° × 1/4° latitude by longitude resolution, which is incapable of resolving smaller scale processes in coastal regions, especially nearshore, that experience high variability and short autocorrelation length scales (Jones et al., 2012). Interpolation techniques, which lack transparency, also rarely probe internal relationship dependency between variables.

Large heterogeneity in air-sea CO₂ fluxes exists in the coastal Northeast Pacific, with substantial expanses of the coast completely devoid of observations (Benway et al., 2016). Large discrepancies exist between previous air-sea CO₂ flux estimates within this region, with disagreement over the net annual flux magnitude and direction (i.e., as a net sink or source for atmospheric CO₂; Duke, Richaud, et al., 2023; Fennel et al., 2019). Air-sea CO₂ flux variability in the region is heavily impacted by coastal processes such as upwelling, river plumes, tidal mixing, and coastal currents (Evans & Mathis, 2013; Evans et al., 2012, 2019; Hales et al., 2005; Ianson et al., 2003; Nemcek et al., 2008). Upwelling along the Pacific eastern boundary shelf has contrasting impacts on the oceanic CO₂ sink reflected in complex interactions between biological carbon drawdown fueled by upwelled nutrient and carbon-rich waters (Hales et al., 2005; Messié & Chavez, 2015; Ribalet et al., 2010) and outgassing associated with the same subsurface waters brought to the surface (Chan et al., 2017; Christensen, 1994; Evans et al., 2011; Feely et al., 2008; Hales et al., 2005; Ianson & Allen, 2002). Closer to shore, within the Salish Sea, and along Alaska's Inside Passage, air-sea CO₂ fluxes into and out of the ocean are highly episodic and spatially heterogeneous (Evans et al., 2022; Jarníková, Ianson, et al., 2022). Binning regional *p*CO₂ observations in three dimensions into monthly, 1/12° × 1/12° grid cells over the period 1998–2019 (same gridded resolution as created continuous *p*CO₂ product; Section 2), reveals the data scarcity (Figure 1). Of the 6,030,816 spatial and temporal grid cells just 0.6% have an associated gridded *p*CO₂ value. Observations are concentrated along shipping lanes, have a summer bias, and increase in frequency during later years (Figure 1). No observations exist in vast areas of the coastal Gulf of Alaska and along extensive stretches of shoreline (Figure 1c).

Here we investigate how well a high-resolution regional artificial neural network (ANN) approach can determine air-sea CO₂ fluxes in the coastal Northeast Pacific (NEPc). We build on an existing global setup (Landschützer et al., 2013) adopted previously in stepping to a higher spatial resolution in the open Northeast Pacific (Duke et al., 2023b). In Section 2, we describe the creation of a gridded *p*CO₂ data product for the coastal Northeast Pacific monthly from January 1998 to December 2019 at an unprecedented 1/12° × 1/12° resolution to resolve coastal ocean processes. In Section 3, we demonstrate that our product robustly recreates gridded observation data, comparable to a less variable open ocean product. In Section 4, we directly compare our *p*CO₂ product with in situ shipboard and mooring observations and detail potential capabilities and limitations in the continuous, gridded product. In Section 5, we examine the regional patterns of variability in the net annual air-sea CO₂ flux relative to the seasonal cycle and describe potential drivers through a spatial sensitivity analysis. We conclude by calculating surface ocean *p*CO₂ trends in the last decades.

2. Data and Methods

We created a coastal *p*CO₂ data product spanning a geographic area within 45°N–62°N 120°W–155°W and from 6 to 300 km offshore, building on the methods of Duke et al. (2023b) (ANN-NEPc; Duke et al., 2024). Briefly, our first step identified grid cells with similar environmental characteristics, provinces, using a self-organizing map approach (SOM) (Landschützer et al., 2013). In the second step, within each province, we used a feed-forward neural network (FFN) to create non-linear functional relationships between *p*CO₂ observations and

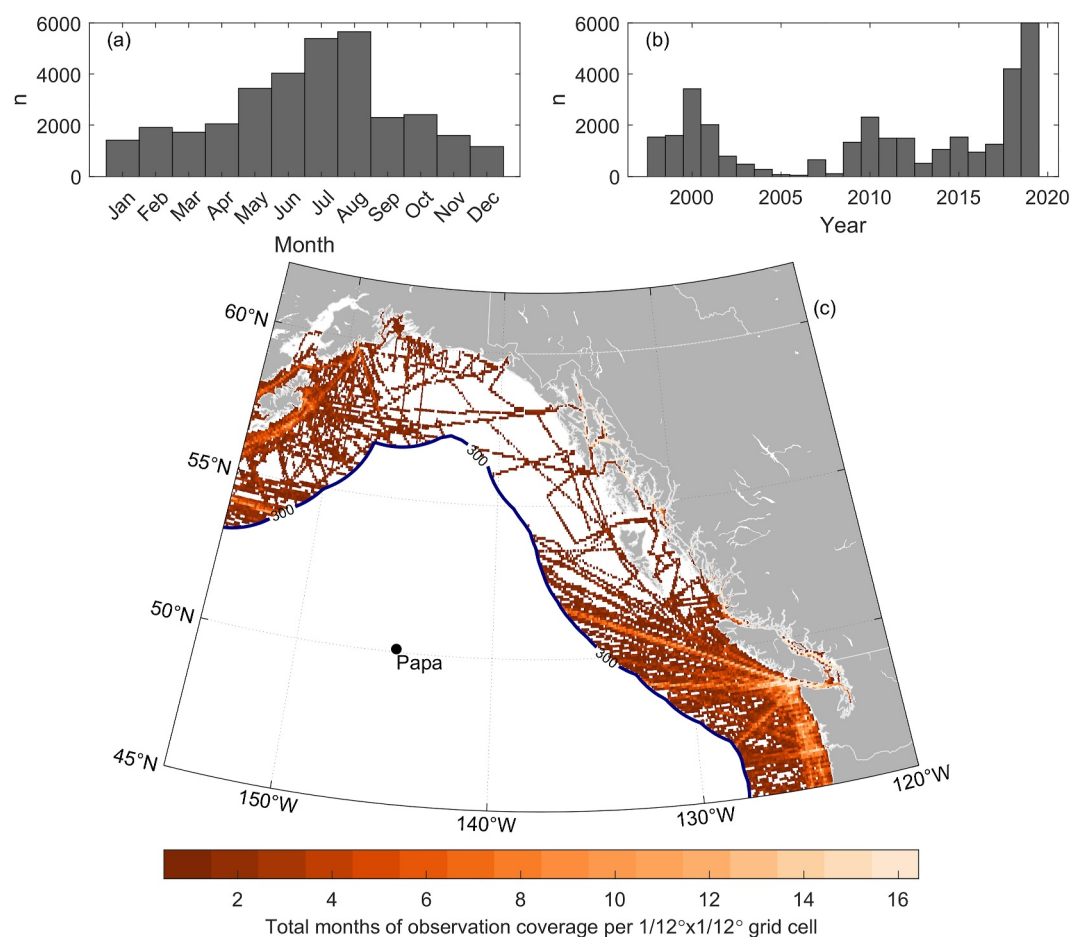


Figure 1. Number of grid cells (of 54,782 total spatial grid cells) with coastal $p\text{CO}_2$ observation data (Section 2.1) in (a) months reveals a summer bias, and (b) years showing increased sampling closer to present. (c) Total number of months of observational coverage per grid cell displays better coverage along shipping routes. 300 km offshore line shown for coastal/open oceanic boundary used in this study (solid blue line labeled “300”).

independent predictor variables (Landschützer et al., 2013). Third, we applied these relationships to the predictor data to generate continuous monthly sea surface $p\text{CO}_2$ maps from 1998 to 2019 in the coastal Northeast Pacific (NEPc). ANN-NEPc fills the gap between open ocean (>300 km offshore) $p\text{CO}_2$ (Duke et al., 2023b) to as close to the shoreline as reanalysis and satellite-based products reach. In stepping to 1/12° spatial resolution (approximately 9 km latitude by 5 km longitude), this work represents a three times increase in spatial resolution over previous 1/4° global and regional coastal ocean products with an overlapping domain (Landschützer et al., 2020; Laruelle et al., 2017; Roobaert et al., 2024; Sharp et al., 2022), with extended coverage into the nearshore (defined here as 0–25 km offshore). The increased resolution derives from high-resolution predictor data used to create the product and available in situ measurements (Table 1; Figure 1).

2.1. $p\text{CO}_2$ Observations

ANN target $p\text{CO}_2$ data came from the Surface Ocean CO₂ Atlas (SOCAT) v2021 (Bakker et al., 2016), the Fisheries and Oceans Canada February 2019 Line P cruise (<https://www.waterproperties.ca/linep/>), a West Coast Ocean Acidification cruise from July and August 2010 (Evans et al., 2012), and La Perouse cruises from May 2007 and May 2010 (Tortell et al., 2012). Sea surface CO₂ fugacity ($f\text{CO}_2$) was converted to sea surface $p\text{CO}_2$ (Text S1 in Supporting Information S1; Körtzinger, 1999). We did not correct in situ $p\text{CO}_2$ observations to sea surface mass boundary layer temperature, because following previous techniques introduced significant additional uncertainty in our coastal study area (Text S2 in Supporting Information S1). $p\text{CO}_2$ observations were bin-

Table 1
Northeast Pacific Coastal Ocean Artificial Neural Network Predictor Variables, and Their Corresponding Source, Original Temporal, and Spatial Resolutions, and Processing Steps Used for This Study

Predictor variable	Source	Original resolution		Processing
		Temporal	Spatial	
Satellite-based product				
Sea surface temperature (SST)	SST_cci: Level 4 Analysis Climate Data Record, version 2.1	Daily	1/20° × 1/20°	Averaged to monthly, aggregated to 1/12° × 1/12°
Chlorophyll- <i>a</i> (Chl)	Ocean_Color_cci: Version 5.0	Daily	1/24° × 1/24°	Averaged to monthly, aggregated to 1/12° × 1/12°, log10-transformed
Satellite and in situ observation data assimilated reanalysis product				
Sea surface salinity (SSS)	Copernicus Marine Service GLOBAL_REANALYSIS_PHY_001_030	Monthly	1/12° × 1/12°	None
Sea surface height (SSH)				None
Atmospheric-measurement-based interpolation product				
Atmospheric <i>p</i> CO ₂	Jersild et al. (2017)-NCEI Accession 0160558	Monthly	1° × 1°	Interpolated to 1/12° × 1/12°
High-resolution regional forecast model				
Wind speed	Regional Deterministic Reforecast System (RDRS-v2.1)	Hourly	1/11° × 1/11°	Averaged to monthly, interpolated to 1/12° × 1/12°

averaged to match predictor resolution for robust FFN training (monthly from 1998 to 2019, at $1/12^\circ \times 1/12^\circ$), computing the mean and standard deviation within each grid cell.

2.2. Predictor Data

Predictor data were chosen based on accessibility and ability to represent processes that mechanistically impact surface ocean $p\text{CO}_2$ (Table 1). Selected predictor variables primarily originate from satellite observations or reanalysis models (Table 1; Text S3 in Supporting Information S1). Predictors differ slightly from a regional open ocean estimate (Duke et al., 2023b). Here, we used a high-resolution regional wind speed product and not reanalysis model derived mixed layer depth. Capturing greater variability in the coastal ocean required a high-resolution regional wind speed product over a low-resolution global product (Figure S2 in Supporting Information S1). Latitude, longitude, and time were not used as predictor variables.

2.3. Neural Network Construction

To reach the optimal ANN-NEPc architecture, we performed a series of tuning tests using the MATLAB Neural Network Toolbox, with sequential improvements impacting future tests (Duke et al., 2023b). The choice of three dynamic (i.e., changing shape at every timestep) SOM based clusters represented the lowest number for a typical clustering structure to emerge (supplementary Figure S3a in Supporting Information S1). All spatial grid cells within the study area belong to more than one SOM cluster at some point over 1998–2019 (Figure S3b in Supporting Information S1). SOM predictor variables (sea surface temperature (SST), sea surface salinity (SSS), sea surface height (SSH) only; Table 1) were normalized to a mean of 0 and standard deviation of 1. The second FFN step used all six predictor variables in Table 1, in addition to each predictor variable anomaly (i.e., deseasonalized; calculated by subtracting the climatological monthly mean), bringing the total number of predictors to 12. Anomaly values were used to highlight interannual to decadal variability within our predictor data sets. The number of neurons within the first hidden layer varied by province with the optimal number of neurons determined in a pre-training run (Landschützer et al., 2013, 2014). The second hidden layer used seven static neurons, which slightly improved performance by up to $5 \mu\text{atm}$ compared to independent measurement (Section 3.3). To further decrease the risk of overfitting, we used a 10-fold cross-evaluation approach to create an ANN ensemble (Duke et al., 2023b; Li et al., 2019, 2020) and a bootstrapping method (Landschützer et al., 2013). Observation cruises were randomly divided into 10 equal subsamples (10% each) using expocodes (i.e., unique identifiers corresponding to complete underway cruise tracks or mooring deployments) prior to gridding, leaving some data splits with more (or less) gridded $p\text{CO}_2$ targets (Section 2.1). We repeated the FFN training step 10 times, using each of the 10 subsamples once as the internally withheld evaluation data set and the rest as the training data set (with a separate independent data always withheld; Section 2.4). In each iteration, we trained the ANN for 10 rounds. The robustness and reliability of an ANN estimate has been shown to be significantly improved by combining an ANN ensemble (Duke et al., 2023b; Fourrier et al., 2020; Linares-Rodriguez et al., 2013; Sharkey, 1999). Here, we take the mean of the 10-fold estimates.

2.4. Evaluation

Comparisons of ANN output to training and independent withheld data were made throughout tuning tests. ANN-NEPc performance for each tuning test was evaluated using five statistical metrics: root mean squared error (RMSE), coefficient of determination (r^2), mean absolute error (MAE), mean bias (calculated as the mean residual), and the slope of the linear regression (c_1) between the ANN and the corresponding gridded $p\text{CO}_2$ observations. One subset of data was selected from the observation data using associated expocodes to be entirely withheld from the FFN training step. We tested 100 random independent withheld data splits and selected the one with the best observational coverage over a wide range of seasons, years, and locations (Figure S4 in Supporting Information S1). These independent withheld data represented approximately 4.5% of the total study area gridded $p\text{CO}_2$ data.

2.5. Sensitivity Analysis

We used a perturbation approach to quantitatively assess the impact of each predictor variable on estimated $p\text{CO}_2$ (e.g., Broullón et al., 2018; Li et al., 2020; Sun et al., 2021). To diagnose how important different predictor variables were across the study area, a single set of non-linear relationships was used inside a single uniform SOM

cluster. We then applied this single FFN to our continuous, gridded predictor data set and to perturbed versions of that data set. For each predictor variable separately, we introduced a perturbation increasing the value within each grid cell by 50% of the standard deviation within that grid cell ($X' = X + 0.5(std(X))$); $N = 264$ months per grid cell; de Oña & Garrido, 2014) and calculated the resulting predicted pCO_2 . We then took the difference between the perturbed run and a baseline run using unperturbed predictor variables.

2.6. Computation of Air-Sea Fluxes

Using our pCO_2 product, we calculated the air-sea CO_2 flux (FCO_2 ; $mol\ m^{-2}\ yr^{-1}$):

$$FCO_2 = K_0 k \Delta pCO_2, \quad (1)$$

from the Henry's Law solubility constant (K_0 ; $mmol\ m^{-3}\ \mu atm^{-1}$) as a function of temperature and salinity (Table 1; Weiss, 1974), gas transfer velocity (k ; $m\ day^{-1}$), and the gradient between pCO_2 in the surface ocean and the atmosphere (ΔpCO_2 ; μatm). Here, the gas transfer velocity is derived from Wanninkhof (2014), a function of wind-speed at 10 m elevation (Table 1) and the temperature dependent Schmidt number specific to CO_2 (Wanninkhof, 2014). Negative flux values indicate CO_2 uptake by the ocean. We assume that the uncertainty in our air-sea CO_2 flux estimate results from a 20% uncertainty in k (Wanninkhof, 2014) and the overall product uncertainty in estimated pCO_2 (θpCO_2 ; Section 3.3 below). As the uncertainty of ΔpCO_2 is dominated by the uncertainty in estimated surface ocean pCO_2 , we neglect the contribution from atmospheric CO_2 despite potential point source effects nearshore (Palter et al., 2023). In our study area there are minimal industrial sources along much of the coastline, prevailing westerlies, monthly averaging, and air-sea disequilibrium is most often large nearshore (e.g., Salish Sea; Section 5.1). In addition, existing atmospheric pCO_2 products are not designed to capture nearshore biases (e.g., Wu et al., 2024). Wind speed product uncertainty, which would contribute to a larger overall flux uncertainty, is not included. This uncertainty is difficult to evaluate in the nearshore where the standard deviation of global wind speed products (Atamanchuk et al., 2020; Roobaert et al., 2018) is likely not an appropriate measure of the uncertainty of our chosen coastal-specific wind product that we use (Figure S2 in Supporting Information S1).

3. Network Performance

3.1. Evaluation With Respect to Observational Data

Comparing our estimated pCO_2 product with the gridded observations across both the training data (Figure 2a) and independent withheld data (Figure 2b) demonstrates fits with an MAE less than 30 μatm and RMSE of around 40 μatm . The mean bias is negligible over the full range ($<0.2\ \mu atm$, smaller than observational uncertainty; Section 3.3). 70% of the calculated residuals fall within the -20 to 20 μatm range, while 47% of the grid cells have absolute residuals $<10\ \mu atm$ especially further offshore (Figure S5 in Supporting Information S1). Despite biases in the seasonal and annual coverage of the observations (Figure 1; Section 2.1), our product performs similarly across different months and years (Table S1 in Supporting Information S1). The ANN ensemble model mean demonstrated improved performance compared to each individual ensemble member (Text S4 in Supporting Information S1). Overall, individual ensemble members showed relatively little deviation (RMSE $<25\ \mu atm$) from the ensemble mean (Figure 2c).

Larger bias exists at the upper and lower limits of the gridded pCO_2 observational range. Our product underestimates pCO_2 observations greater than the 90th percentile ($>412\ \mu atm$; mean bias = $-28\ \mu atm$), and overestimates values less than the 10th percentile ($<306\ \mu atm$; mean bias = 13 μatm). The spatial structure of the residuals reflects this bias distribution (Figure S5 in Supporting Information S1), with negative residuals in the strong mixing regions of the Salish Sea commonly characterized by high pCO_2 (Evans et al., 2012, 2019; Jarníková, Ianson, et al., 2022), and positive residuals along the upwelling zone off the west coast of Washington State, and Oregon characterized by low pCO_2 (Evans et al., 2011). Observation-based pCO_2 products commonly overestimate pCO_2 in highly biologically productive coastal upwelling regions (Chau et al., 2022; Hales et al., 2012; Roobaert et al., 2024; Sharp et al., 2022). Chlorophyll (Table 1) as a proxy for biological productivity in training may not fully represent biological control on pCO_2 . Ford et al. (2022) showed that in regions with high biological activity and nutrients supplied from depth (i.e., South Atlantic upwelling mesoscale eddies) regional, algorithm-derived net community production estimates (Ford et al., 2021) improved ANN pCO_2 estimates.

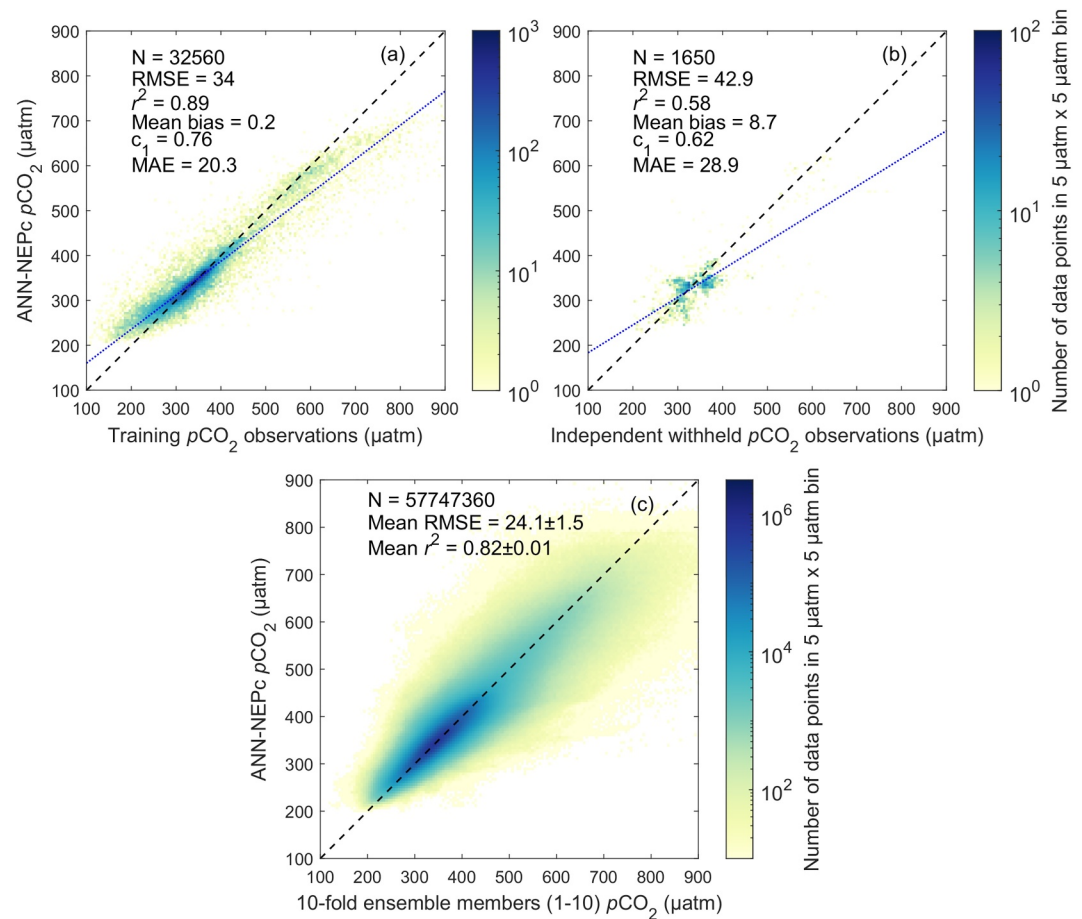


Figure 2. Our ensemble mean $p\text{CO}_2$ estimate (ANN-NEPc) against (a) observed $p\text{CO}_2$ training data, (b) observed $p\text{CO}_2$ independently withheld data, and (c) individual ensemble member estimates. Data are binned into $5 \mu\text{atm}$ by $5 \mu\text{atm}$ bins with data density shown in the colorbar on a log scale (note order of magnitude difference between panels). Dashed black line is the 1:1. Dotted blue line is the least squares best fit. Also shown are number of observations (N), root mean squared error, coefficient of determination (r^2), mean bias (calculated as the mean residual), the slope of the linear regression (c_1), and mean absolute error.

Creation of coastal, regionally specific net community production algorithms, and inclusion as a predictor variable, may help reduce bias of low $p\text{CO}_2$ values in our study area.

In relative terms, our $p\text{CO}_2$ product performs nearly as well as an open ocean product, even nearshore (Table 2). Nearshore $p\text{CO}_2$ exhibits a much larger range of variability compared to the continental shelf and the offshore marine environment. Table 2 displays relative percent error (RPE) binned by distance offshore (d) calculated as:

$$\text{RPE}_d = \text{RMSE}_d / [\text{prctile}_{95}(p\text{CO}_{2,d}^{\text{obs}}) - \text{prctile}_5(p\text{CO}_{2,d}^{\text{obs}})] \times 100, \quad (2)$$

where RMSE_d is the RMSE from gridded observational data averaged over the distance bin, $\text{prctile}_{95}(p\text{CO}_{2,d}^{\text{obs}})$ is the 95th percentile observed $p\text{CO}_2$ in that distance bin and $\text{prctile}_5(p\text{CO}_{2,d}^{\text{obs}})$ is the 5th percentile. Compared to a high-performance, regional open ocean product (Table 2; Duke et al., 2023a), RMSE increases moving toward shore but so does the range in $p\text{CO}_2$ such that the RPE is constant within a factor of two.

3.2. Comparison to Other Products

Our $p\text{CO}_2$ estimate agrees well with one other Northeast Pacific coastal ocean estimate but diverges from coarser resolution global products (Figure S7 in Supporting Information S1). The regional Sharp et al. (2022) product within the northern extension of the California Current System (45°N to 59°N , east of 140°W) is nearly equivalent

Table 2

Error Statistics for Our Ensemble Mean $p\text{CO}_2$ Estimate Against All Gridded Observation Data Binned by Distance Offshore: Number of Observations (N) per Bin, Observed Range of Variability (Range; Difference Between the 95th and 5th Percentile), Root Mean Squared Error (RMSE), and Relative Percent Error (RPE; Equation 2)

Distance offshore (km)	N	Range (μatm)	RMSE (μatm)	RPE (%)
0–25 (nearshore)	8,669	481	54	11
25–50	4,763	215	33	16
50–100	5,770	153	24	15
100–150	3,324	114	16	14
150–200	3,317	90	12	13
200–300	6,501	106	10	10
High-resolution Northeast Pacific open ocean product (Duke et al., 2023a)				
>300	34,096	83	7	8

to our $p\text{CO}_2$ product within reported uncertainties ($r^2 = 0.57$; Figure S7a in Supporting Information S1). However, our product produces estimates closer to shore (Section 5.2 below). Compared to our product and in situ observations, a global coastal climatology (Landschützer et al., 2020; Laruelle et al., 2017) and multiyear product (Roobaert et al., 2024) do not capture the same $p\text{CO}_2$ range (Figures S7c, S7e, and S8 in Supporting Information S1). For example, both global products underestimate winter $p\text{CO}_2$ values closer to shore in the coastal Gulf of Alaska region ($>52^\circ\text{N}$ and <50 km offshore; area-averaged climatological winter $p\text{CO}_2$ of 300 and 290 μatm respectively compared to 330 μatm in this study; Figures S7d and S7f in Supporting Information S1), highlighting the importance of finer resolution in coastal systems. This region also has the scarcest $p\text{CO}_2$ observations within our study area (0.37% coverage; Figure 1). Global SOM clusters commonly group the California Current System with the Northwest European shelf and Sea of Japan (Laruelle et al., 2017; Roobaert et al., 2024). FFN non-linear relationships inside such clusters may not be suitable for regionally specific processes dominated by downwelling (Stabeno et al., 2004), glacial runoff (Pilcher et al., 2018; Siedlecki et al., 2017), significant seasonal biological productivity (Coyle et al., 2012; Fiechter & Moore, 2009; Hermann et al., 2009), and the influence of the upwelling subpolar Alaskan Gyre (Duke et al., 2023b; Hauri et al., 2021). This finding supports the Sharp et al. (2022) recommendation of increasing the number of SOM clusters for observation-based coastal ocean $p\text{CO}_2$ estimates to capture more regionally specific non-linear relationships, cognizant of SOCAT observation data density.

3.3. Uncertainty Estimate

Uncertainty in the ANN-NEPc estimated $p\text{CO}_2$ product was determined following Duke et al. (2023b). The overall $p\text{CO}_2$ product uncertainty ($\theta_{p\text{CO}_2} = 50 \mu\text{atm}$ in our coastal product) is calculated from the square root of the sum of the four squared errors (i.e., added in quadrature): observational uncertainty based on reported SOCAT QA/QC flags ($\theta_{\text{obs}} = 3.7 \mu\text{atm}$), gridding uncertainty based on the average standard deviation from gridding observations into monthly $1/12^\circ \times 1/12^\circ$ bins ($\theta_{\text{grid}} = 22.4 \mu\text{atm}$; with an increasing gradient shoreward), ANN interpolation uncertainty based on the RMSE comparing the ANN-NEPc estimated $p\text{CO}_2$ to independent withheld data ($\theta_{\text{map}} = 42.9 \mu\text{atm}$; Section 3.1), and ANN run randomness uncertainty based on the mean standard deviation between 10-fold ensemble members ($\theta_{\text{run}} = 6.8 \mu\text{atm}$; Figure S9 in Supporting Information S1). ANN interpolation uncertainty is the largest contribution overall. Combining the reported uncertainty in the gas transfer velocity (Section 2.6) and the overall $p\text{CO}_2$ product uncertainty yields an average uncertainty of $\pm 0.2 \text{ mol m}^{-2} \text{ yr}^{-1}$ in the air-sea gas flux across all grid cells, with the largest fraction of the error stemming from the uncertainty in the gas transfer velocity.

Our reported total uncertainty may appear high relative to other coastal $p\text{CO}_2$ products, but we include higher variability regions and more stringent error estimates. Other observation-based interpolated $p\text{CO}_2$ products in the coastal ocean report lower uncertainty values (RMSE values generally between 10 and 35 μatm in regional estimates detailed in S. Chen et al. (2016); 29 μatm globally in Roobaert et al. (2024); approximately 30 μatm in the California Current System in Sharp et al. (2022); 55 μatm in the coastal subpolar Pacific in Chau et al. (2022)). However, most other estimates did not use independent withheld data to report total product uncertainty. Roobaert et al. (2024) point out their largest RMSE values are calculated along the Cascadia Shelf in our study area (62 μatm). Our $p\text{CO}_2$ product is also the only estimate that includes the nearshore, introducing higher variability (Table 2). Excluding the nearshore across all components of the uncertainty calculation yields an overall uncertainty of 40 μatm , more comparable to other coastal ocean estimates.

4. Comparison to High-Resolution Observations

Comparison to in situ observations shows that our ANN-NEPc estimated $p\text{CO}_2$ product resolves seasonal variability and broad spatial patterns well. Despite high spatial resolution, our design of a monthly timestep product means the ANN cannot reproduce short temporal (e.g., days) events. Predictor variable inaccuracy also contributes to $p\text{CO}_2$ estimate uncertainty, particularly in the nearshore where data assimilation into reanalysis models

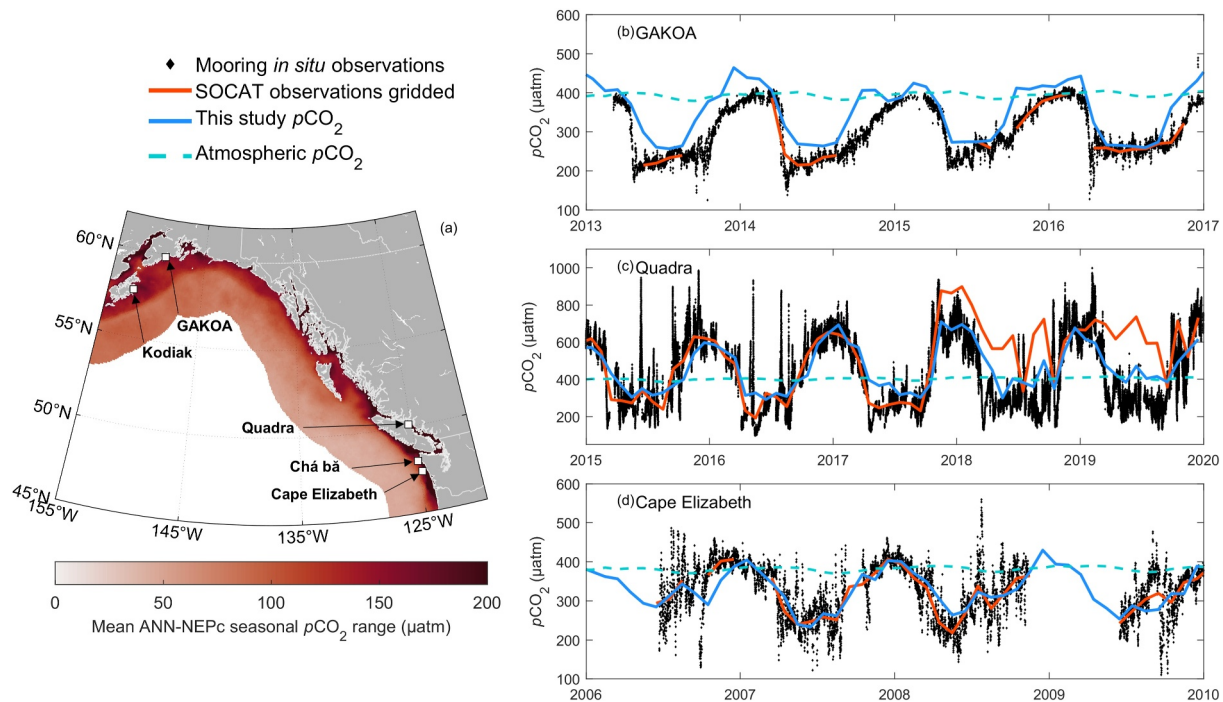


Figure 3. (a) Map of mean estimated surface ocean $p\text{CO}_2$ seasonal amplitude (1998–2019; range; annual maximum minus minimum) in μatm . Nearshore mooring time series at (b) Gulf of Alaska Ocean Acidification mooring, (c) Quadra, and (d) Cape Elizabeth mooring in situ $p\text{CO}_2$ data (black diamonds; not all included in SOCATv2021) plotted with co-located gridded SOCATv2021 (orange solid line), this study $p\text{CO}_2$ (blue solid line), and atmospheric $p\text{CO}_2$ (light blue dashed line). Kodiak and Chá bá and Roobaert et al. (2024) comparison time series in Figure S8 in Supporting Information S1.

is limited (e.g., SSS and coastal limitations of Argo float array) and retrieval issues affect satellite estimates (e.g., SST and cloud masking, impact of aerosols, diurnal variability, uncertainty estimation, and validation). In situ measurements show that biogeochemical and hydrographic variability in our region occurs on spatial scales of less than 20 km (Nemcek et al., 2008), with spatial autocorrelation lengths increasing offshore (Murphy et al., 2001), and timescales of days to weeks (Evans et al., 2011, 2012, 2019; Fassbender et al., 2018). Our product is constrained by initial binning of observations to $1/12^\circ \times 1/12^\circ$ (approximately 9 km by 5 km) and a monthly time step, as well as scarcity of observations used to train (Figure 1). Comparing it directly with in situ mooring and shipboard underway $p\text{CO}_2$ system measurements in the coastal zone provides insight into when and where the ANN is both capable and incapable of resolving variability. This direct data comparison is not intended for evaluation (as in Section 3), but rather to showcase the ability of the ANN to resolve observed $p\text{CO}_2$ variability, given constraints.

Our $p\text{CO}_2$ estimate captures the observed seasonal cycle (phase and amplitude) at regional mooring time series well (Figure 3; full time series at all five regional mooring sites in Figure S8 in Supporting Information S1). At NOAA's Gulf of Alaska Ocean Acidification (GAKOA) site south of Alaska's Kenai Peninsula, our product tends to overestimate seasonal summer minima and winter maxima values (Evans & Mathis, 2013). Our product also predicts an increase that is slightly early with respect to autumn observations, which is potentially due to the lack of autumn data included in SOCAT. However, overall, it captures seasonal cycle timing well with a similar average seasonal amplitude even during times when not all mooring data are included in SOCATv2021 (Figure 3, black points that are not overlain with red) and training data remain scarce (this study average range = 144 μatm ; GAKOA = 169 μatm ; Figure 3b). At another NOAA Gulf of Alaska mooring site south of Kodiak Island, our estimate also captures the phase of the seasonal cycle well ($r^2 = 0.89$; $N = 31$ months; Figure S8a in Supporting Information S1).

The ANN recreates the seasonal cycle well at Hakai Institute's Quadra Island Station, but its monthly timestep does not capture higher frequency variability (Figure 3c). In some instances, measured $p\text{CO}_2$ at the Quadra mooring increases over 500 μatm within 3 days (e.g., 9–12 June 2015), leading to a strong outgassing signal. The ANN monthly estimate does not capture such short events. Monthly binning impacts net annual air-sea CO_2

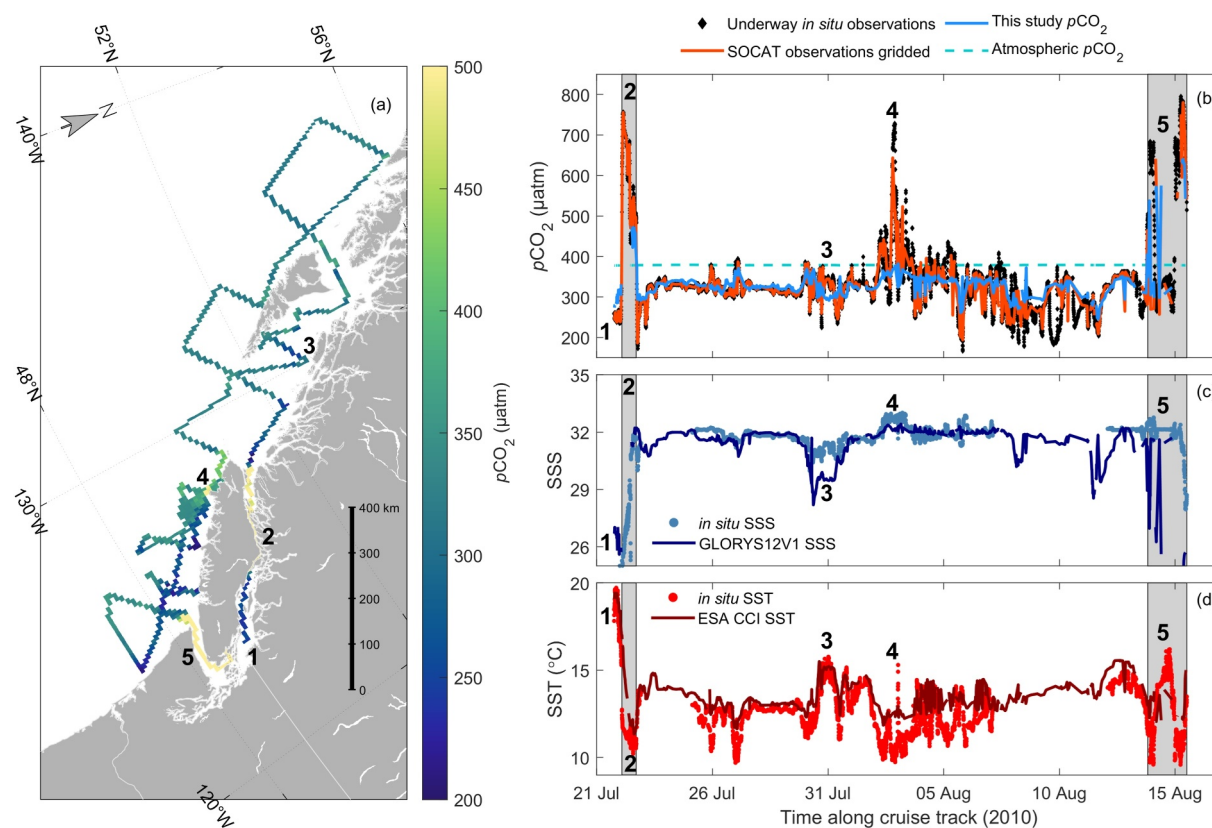


Figure 4. (a) $p\text{CO}_2$ along 2010 West Coast Ocean Acidification cruise track from 21 July 2010 to 15 August 2010 (Evans et al., 2012). Data is gridded into $1/12^\circ$ by $1/12^\circ$ bins. Events indicate (1) cruise start, (2) Johnstone Strait, (3) Hecate Strait, (4) intense upwelling plume near Brooks Peninsula, and (5) Juan de Fuca Strait, respectively. Subplots against time along cruise track for (b) $p\text{CO}_2$ where underway in situ $p\text{CO}_2$ data (black diamonds) are plotted with co-located monthly gridded data (orange solid line), this study $p\text{CO}_2$ (blue solid line), and atmospheric $p\text{CO}_2$ (light blue dashed line). (c) Sea surface salinity (SSS) with underway in situ SSS (light blue dots) and co-located reanalysis SSS (dark blue solid line; used as a predictor variable). SSS values near cruise start as low as 15 in situ and 24 from reanalysis (not shown). (d) Sea surface temperature (SST) with underway in situ SST (red dots) and co-located satellite-based SST (dark red solid line; used as a predictor variable). Gray boxes highlight tidal mixing zones (e.g., Johnstone Strait, Juan de Fuca and Haro Straits and connecting waters).

fluxes within a single grid cell (2015 mean annual flux from daily mooring $p\text{CO}_2$ and wind speed: $0.08 \text{ mol m}^{-2} \text{ yr}^{-1}$; compared to this study: $0.26 \text{ mol m}^{-2} \text{ yr}^{-1}$) but likely has a smaller impact when quantifying the larger regional flux. Near the end of the time series (late 2017 to 2020), the gridded SOCAT data deviates from the in situ mooring data due to inclusion of nearby shipboard data, yet our estimated $p\text{CO}_2$ continues to better represent the mooring seasonal cycle. When evaluating ANN performance (Section 3.1), this difference from the gridded observation data contributes to a higher measure of uncertainty, yet in situ representation is still preserved compared to the mooring data.

The ANN does capture part of the signal from somewhat longer (i.e., weeks) summer high $p\text{CO}_2$ events at NOAA's Cape Elizabeth mooring off the west coast of Washington State (Figure 3d). Horizontal advection of freshwater (July 2007) or upwelling events ($>500 \text{ } \mu\text{atm}$; July 2008; Evans et al., 2015) can cause high summer $p\text{CO}_2$ values. These extreme events impact bin-averaged training data, allowing the ANN to recover some of the short duration signal, albeit at a lower value. Our product reproduces both persistent, weeks long events $<35 \text{ km}$ offshore, in line with the monthly averaged observations.

Direct comparison to a cruise from July/August 2010 provides another example of our $p\text{CO}_2$ product's ability to capture broadscale patterns. The ANN estimate resolves undersaturated $p\text{CO}_2$ conditions in the Salish Sea at the start of the cruise well (point 1; Figure 4). Through Johnstone Strait (50.5°N , 126.5°W), a strong tidal mixing zone (Evans et al., 2022), lack of predictor data coverage prevents estimation of $p\text{CO}_2$ in those grid cells at all (point 2; Figure 4). The ANN captures the lower variability continental shelf and slope environment in Queen Charlotte Sound and around Haida Gwaii well (between points 2 and 4; Figure 4). Differences between estimated and

observed $p\text{CO}_2$ exist in Hecate Strait (point 3; Figure 4) likely due to strong underestimation of SSS as a predictor in the reanalysis product (point 3; Figure 4c). Along the west coast of Vancouver Island, shipboard observations captured an upwelling event off Brooks Peninsula (50.14°N, 127.78°W; Asher et al., 2017), visible in decreased temperatures, elevated salinity, and high in situ $p\text{CO}_2$ (point 4; Figure 4). The ANN does not replicate this short upwelling event (i.e., days; Asher et al., 2017). High $p\text{CO}_2$ driven by tidal mixing in the Juan de Fuca and Haro Straits are captured by the ANN (point 5; Figure 4; Jarníková, Olson, et al., 2022). An abundance of consistently high $p\text{CO}_2$ observations results in a strong reconstruction by the ANN in this region (Evans et al., 2012).

5. Air-Sea CO_2 Flux and $p\text{CO}_2$ Drivers

Long-term (1998–2019) mean air-sea CO_2 fluxes display a pronounced juxtaposition between strong uptake and outgassing regions in the coastal Northeast Pacific Ocean (Figure 5c). Overall, air-sea CO_2 flux estimates from our product show this coastal zone acts as a net sink for atmospheric CO_2 , drawing down $0.96 \pm 0.25 \text{ Tg C yr}^{-1}$ with a mean flux of $-0.7 \text{ mol m}^{-2} \text{ yr}^{-1}$ but high variability with a standard deviation of $1.4 \text{ mol m}^{-2} \text{ yr}^{-1}$. Mean $p\text{CO}_2$ and air-sea CO_2 fluxes display similar patterns, with high $p\text{CO}_2$ nearshore leading to outgassing and low $p\text{CO}_2$ along the transition zone and continental shelf environments taking up atmospheric CO_2 (Figures 5a and 5c). Canada's West Coast exclusive economic zone has a CO_2 uptake of $0.61 \pm 0.11 \text{ Tg C yr}^{-1}$. Compared to the open ocean region of the Northeast Pacific (Duke et al., 2023b), the adjacent coastal ocean is a weaker sink for atmospheric CO_2 by area (40% weaker compared to $-1.2 \text{ mol m}^{-2} \text{ yr}^{-1}$ in the open ocean), taking up 64% less CO_2 total within 40% less area (open ocean uptake = $2.63 \pm 0.53 \text{ Tg C yr}^{-1}$; open ocean surface area = $1.8 \times 10^6 \text{ km}^2$; coastal ocean surface area = $1.1 \times 10^6 \text{ km}^2$). Elevated $p\text{CO}_2$ and outgassing is also reported in the subpolar Alaskan Gyre system (Figures 5a and 5c), consistent with Duke et al. (2023b).

5.1. Regional Patterns

Spatially, the study area can be divided into four distinct regions based on air-sea CO_2 flux patterns in our product. The net annual air-sea CO_2 flux is anti-correlated with the mean air-sea CO_2 flux seasonal amplitude ($r^2 = 0.56$; $p < 0.01$; Figure 5e). We identify four regions that drive this pattern from most offshore to inshore: the transitional zone connecting the open ocean and the coast is a net sink with a small seasonal cycle, the Cascadia Shelf where the net sink is even stronger but the seasonal cycle remains low, nearshore regions with large seasonal cycles, and semi-enclosed estuaries with strong outgassing. To further disentangle driving processes between these four regions we decompose the estimated $p\text{CO}_2$ into a thermal ($p\text{CO}_{2(\text{T})}$) and biophysical ($p\text{CO}_{2(\text{BP})}$) component (Text S5 in Supporting Information S1; Takahashi et al., 1993, 2002). We then take the ratio ($R_{\text{T BP}}^{-1}$) of the seasonal amplitude (climatological maximum minus minimum) of the two components ($p\text{CO}_{2(\text{T})}/p\text{CO}_{2(\text{BP})}$; Figure 5b), where biophysical processes dominate if $R_{\text{T BP}}^{-1}$ is less than one and vice versa.

Much of the offshore transitional zone (medium blue colors, closer to 300 km offshore coastal/open oceanic boundary in Figure 5c) acts as a sink for atmospheric CO_2 year-round where thermal and biophysical $p\text{CO}_2$ components are nearly balanced. Low air-sea CO_2 flux seasonal amplitudes in the transitional zone (>50 km offshore; excluding the subpolar Alaska Gyre) correspond to net annual atmospheric CO_2 uptake. In the southeast of the study area (Figure 5b), the North Pacific Current region experiences a relative balance of opposing thermal and biophysical $p\text{CO}_2$ components seasonally ($R_{\text{T NT}}^{-1}$ approximately = 1; Duke et al., 2023b; Sutton et al., 2017; Takahashi et al., 2006; Wong et al., 2010). Along most of the transitional zone where $R_{\text{T NT}}^{-1}$ is closer to one (Figure 5b), we also report low $p\text{CO}_2$ seasonal amplitudes (Figure 3a) allowing for continuous $p\text{CO}_2$ undersaturation with respect to the atmosphere and continuous annual uptake with low air-sea CO_2 flux seasonal amplitudes (Figure S12 in Supporting Information S1; Figure 5d). Advection of low $p\text{CO}_2$ (Duke et al., 2023b; Takahashi et al., 2006) water by the North Pacific Current from the open ocean toward the coast causes overall $p\text{CO}_2$ undersaturation in this region (Reed & Schumacher, 1986; Thomson, 1981; Weingartner et al., 2002). The low $p\text{CO}_2$ amplitudes are maintained by the effect of temperature on $p\text{CO}_2$ (increasing during warming and decreasing during cooling) dampening changes due to spring phytoplankton blooms (drawing down $p\text{CO}_2$) and winter surface mixed layer deepening (increasing $p\text{CO}_2$).

The most prominent CO_2 sink region is found along the Cascadia Shelf, inshore of the transitional zone, with a mean flux of $-1.5 \text{ mol m}^{-2} \text{ yr}^{-1}$ (darkest blue colors along West Coast Vancouver Island, Washington State, and Oregon in Figure 5c). Along the continental shelf and within much of the nearshore, biophysical processes (e.g., coastal upwelling, seasonal biological drawdown, mixing) dominate the seasonal cycle of $p\text{CO}_2$ with $R_{\text{T NT}}^{-1}$

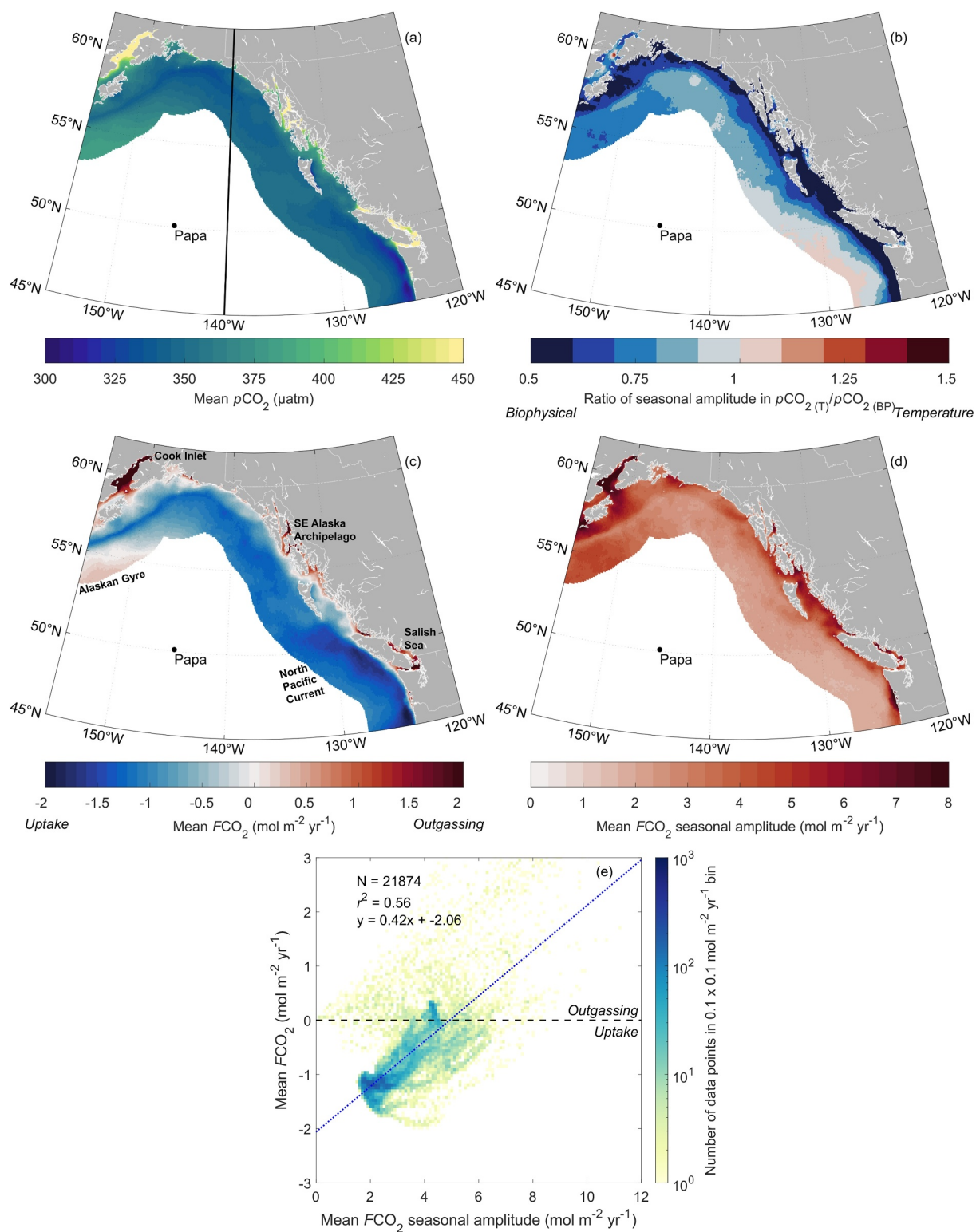


Figure 5.

values < 1. Summer upwelling fuels primary productivity causing surface $p\text{CO}_2$ drawdown as waters are advected offshore (Hales et al., 2005; Teeter et al., 2018; Ware & Thomson, 2005). Winter downwelling drives onshore transport of low $p\text{CO}_2$ offshore waters and prevents subsurface waters, with elevated respiratory CO_2 , from mixing to the surface (i.e., coastal nutrient trap; Ianson et al., 2009; Wilkerson & Dugdale, 1987; Whitney et al., 2005). This general circulation of shelf waters maintains low seasonal flux amplitudes and strong CO_2 uptake on the Cascadia Shelf.

Much of the nearshore tends to experience seasonally strong, juxtaposing air-sea CO_2 fluxes, leading to near zero net annual CO_2 fluxes (nearshore white colors in Figure 5c). For example, closer to shore north of 50°N and south of the Southeast Alaska Archipelago, winter mixed layer deepening brings water rich in nutrients and CO_2 from respired organic matter to the surface, increasing $p\text{CO}_2$, leading to strong CO_2 outgassing to the atmosphere when light is limiting (Figure S12a in Supporting Information S1; Marchese et al., 2022). In the spring and summer, substantial primary productivity draws down $p\text{CO}_2$ (Marchese et al., 2022), reverting the region to a prominent sink for atmospheric CO_2 (Figures S12b and S12c in Supporting Information S1). This large seasonal amplitude results in a net neutral flux.

Semi-enclosed, nearshore estuarine environments display strong CO_2 outgassing in our product, that is not always observed in regional high-resolution models. High $p\text{CO}_2$ values and outgassing fluxes (mean CO_2 flux of $0.7 \text{ mol m}^{-2} \text{ yr}^{-1}$) occur in Cook Inlet, the Salish Sea, and the Southeastern Alaska Archipelago (Figure 5c). Globally, the source strength of these integrated estuarine environments is comparable to (or smaller than) other nearshore source regions that decrease averaged coastal ocean CO_2 uptake (Section 5.2 below; Duke, Richaud, et al., 2023; Fennel et al., 2019; Laruelle et al., 2018). In high-resolution regional models, the Salish Sea has been reported as a weak net annual source (this study: $1.0 \text{ mol m}^{-2} \text{ yr}^{-1}$; comparable to Jarníková, Ianson, et al. (2022): $0.69 \text{ mol m}^{-2} \text{ yr}^{-1}$), and Cook Inlet as a net sink (Hauri et al., 2020; Pilcher et al., 2018). Limited observations used to constrain both our observation-based estimate and regional models may create discrepancies between them. Our estimate is based on all available surface ocean $p\text{CO}_2$ observations along with a suite of predictor variables (Figure 1; Table 1), whereas regional process-based models using data for boundary conditions simplify and parameterize mechanisms (Hauri et al., 2020; Jarníková, Ianson, et al., 2022; Pilcher et al., 2018). Global observation-based estimates and models also disagree, where model fluxes are often more negative (stronger sink) at northern latitudes, attributed to a smaller seasonal $p\text{CO}_2$ amplitude (Resplandy et al., 2024).

5.2. Nearshore Fluxes

The nearshore coastal environment (0–25 km offshore) exhibits large air-sea CO_2 fluxes, over a relatively small surface area, impacting regional marine carbon budgeting. As our estimate wraps around the coast from primarily E-W to primarily N-S, we split the region along the 140°W meridian (Figure 5a). Averaging grid cells approximately parallel to the regional coastline along longitudinal bands (155°W to 140°W west of 140°W ; Figures 6a and 6b) and along latitudinal bands (56°N to 45°N east of 140°W ; Figures 6c and 6d), the inclusion or exclusion of the nearshore environment creates large differences in estimated net annual air-sea CO_2 fluxes, for example, between 154°W and 149°W encompassing Cook Inlet (absolute flux difference of 250%, switching from a net sink to a source; Figure 6b). North to south from 56°N to the northern extension of the California Current System at 45°N (Figure 6d), including the nearshore leads to a slightly weaker net annual sink for atmospheric CO_2 . The difference is largest within latitudinal bands inclusive of the Salish Sea ($49\text{--}51^\circ\text{N}$; 20% weaker). Differences in zonally averaged $p\text{CO}_2$ and air-sea CO_2 fluxes also exist between products with varying nearshore coverage (Section 3.2; Roobaert et al., 2024; Sharp et al., 2022). Inclusion of the nearshore changes the annual exchange with the atmosphere within the study area by $0.06 \text{ Tg C yr}^{-1}$ (6%). These results highlight the importance of including the nearshore in regional marine carbon budgets.

Figure 5. (a) Mean $p\text{CO}_2$ (1998–2019) in μatm . 140°W meridian divide used in Section 5.2 analysis shown for reference. (b) Ratio of $p\text{CO}_2$ seasonal amplitude in thermal component (i.e., changes due to temperature; $p\text{CO}_{2(T)}$) and biophysical component (i.e., changes due to circulation, mixing, gas exchange, and biology; $p\text{CO}_{2(BP)}$). (c) Mean air-sea CO_2 flux (1998–2019) in $\text{mol m}^{-2} \text{ yr}^{-1}$. Negative flux values indicate CO_2 uptake by the ocean. (d) Mean air-sea CO_2 flux seasonal amplitude (range; annual maximum minus minimum) in $\text{mol m}^{-2} \text{ yr}^{-1}$. (e) Mean air-sea CO_2 flux versus mean air-sea CO_2 flux seasonal amplitude (grid cell by grid cell). Dotted blue line is the least squares best fit. Dashed black line separates values of outgassing (positive) from uptake (negative). Alaskan Gyre and North Pacific Current labels indicate the approximate location where these circulation features impinge on the study area (Franco et al., 2021).

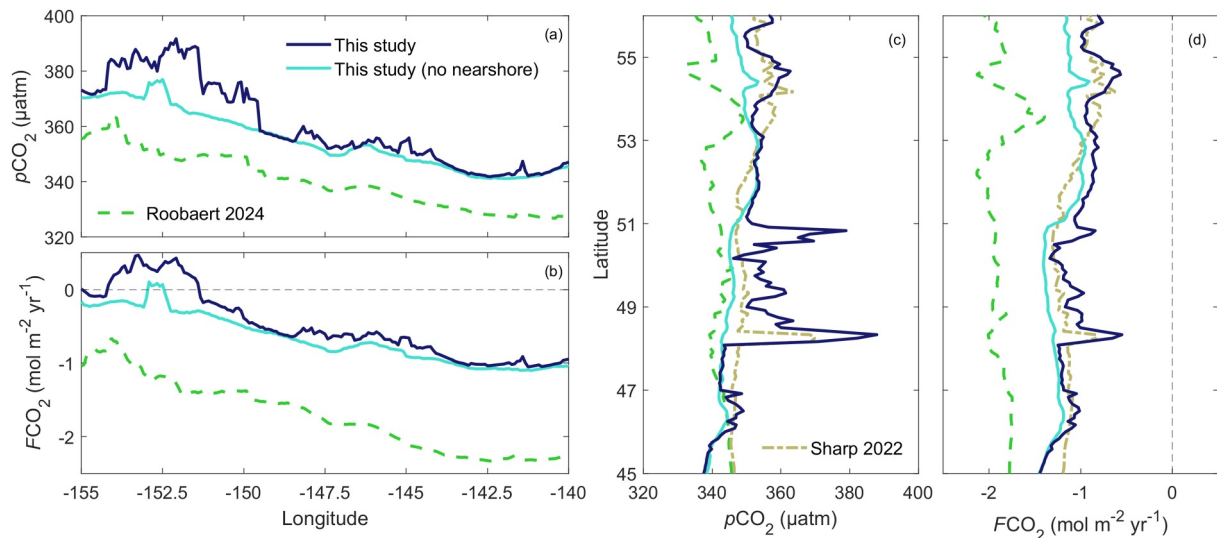


Figure 6. Longitudinally averaged estimates west of 140°W of mean (a) $p\text{CO}_2$ and (b) air-sea CO_2 flux of: this study (dark blue), this study removing the nearshore (cyan). Panels (c, d) are latitudinally averaged estimates east of 140°W respectively. Additional observation-based estimates with overlapping domains (1998–2019) including: Sharp et al. (2022) (dot-dash beige), and Roobaert et al. (2024) (dashed lime green). Sharp et al. (2022) air-sea CO_2 fluxes calculated following Section 2.6.

5.3. Dominant Controls on Variability

Four distinct tiers of predictor variable importance rankings emerged from a perturbation-based spatial sensitivity analysis in estimated $p\text{CO}_2$ (Figure 7a). The ANN is purely a set of empirical, not mechanistic, relationships between $p\text{CO}_2$ observations and predictor variables, though variables were selected with mechanism in mind (Table 1). We used a perturbation-based spatial sensitivity analysis (Section 2.5) to probe the dependency of the ANN relationships on each variable, as they cannot be viewed directly (unlike a multiple linear regression). Atmospheric $p\text{CO}_2$ and atmospheric $p\text{CO}_2$ anomaly (removing the seasonal cycle; Section 2.2) are the most important predictors, followed by SST, and then process-driven controls whose importance varies spatially. Atmospheric $p\text{CO}_2$ and atmospheric $p\text{CO}_2$ anomaly are the only two predictor variables that capture a trend in time from 1998 to 2019 (i.e., increase of $2.12 \mu\text{atm yr}^{-1}$ due to anthropogenic emissions). Due to the trend, these variables also experienced the largest absolute value perturbation (mean study area wide increase of $7 \mu\text{atm}$), at least one order of magnitude greater than other variables. The third most important predictor for estimating $p\text{CO}_2$ is SST. Study area wide, the sensitivity test introduced a mean SST increase of 1.5°C , resulting in a mixed $p\text{CO}_2$ response where generally there was a decrease, outside of the Gulf of Alaska central glacial drainage basin where $p\text{CO}_2$ increased (Figure S13a in Supporting Information S1). This result does not follow the mechanistic reduced solubility of CO_2 in warmer water. However, it emphasizes the importance of the SST seasonal cycle as a predictor (strong correlation, typically negative, between $p\text{CO}_2$, and SST; Figure S13b in Supporting Information S1).

Excluding the three most dominant controls (atmospheric $p\text{CO}_2$, atmospheric $p\text{CO}_2$ anomaly, and SST), the spatial distribution of predictor variable importance rankings can be explained by mechanistic drivers even though the ANN is purely empirical. SSH anomaly is important along the Alaskan Gyre boundary, where the upwelling gyre exerts control over local biogeochemistry (Figure 7b; Duke et al., 2023b; Hauri et al., 2021). Wind speed (as a proxy for mixed layer depth) is important throughout most regions along the continental shelf and the outer coast as winter mixed layer deepening brings CO_2 -rich subsurface waters to the surface (a mean study area wide perturbation increase of 0.4 m s^{-1} resulted in a $p\text{CO}_2$ increase of 1.7% from the baseline; Figure 7b). SSH and SSH anomaly are additionally important offshore of Sitka, Alaska (57°N , 143°W) and Haida Gwaii (52°N , 133°W) where mesoscale anticyclonic eddies with enhanced primary productivity and high SSH propagate away from the continental margin (Figure 7b; Batten & Crawford, 2005; Crawford & Whitney, 1999; Crawford et al., 2007; Whitney & Robert, 2002; Whitney et al., 2005). In the North Pacific Current influenced region southeast of the study area, SST anomaly and wind speed anomaly are the most important predictors linked to the relative balance of opposing mechanisms (i.e., thermal and biophysical $p\text{CO}_2$ components; Figure 5b).

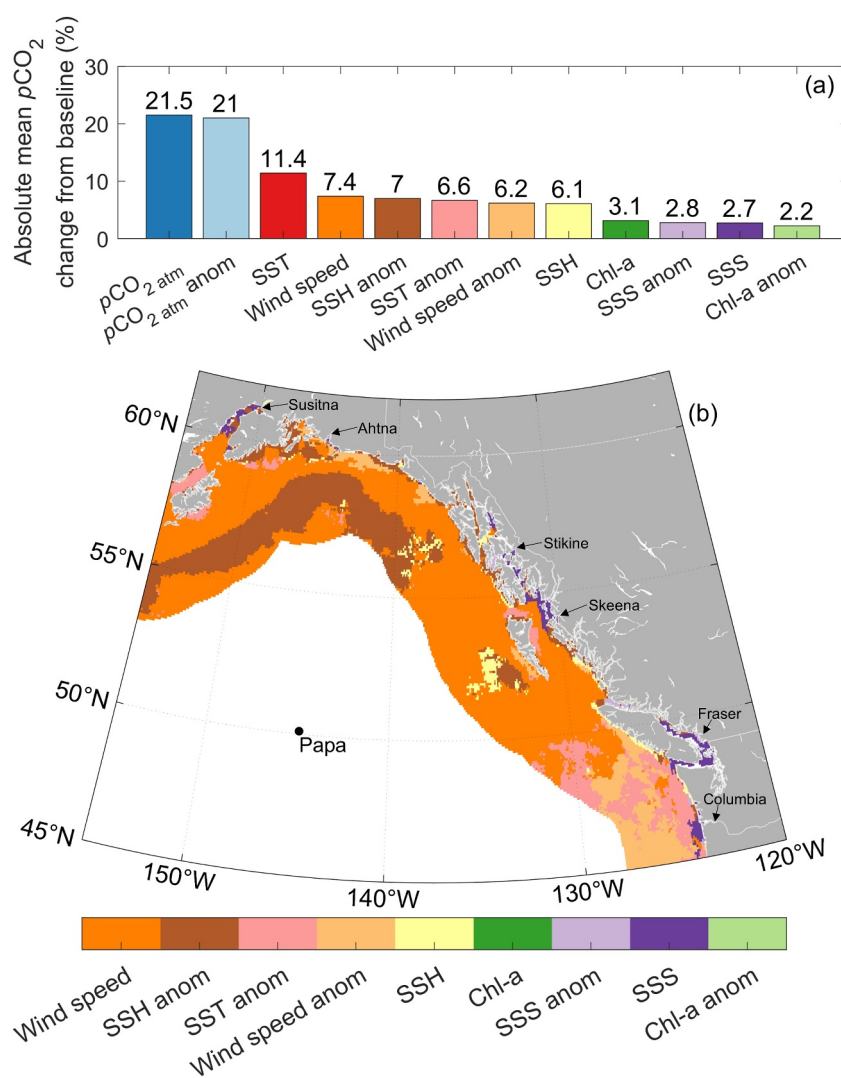


Figure 7. (a) Predictor variables ordered by absolute mean $p\text{CO}_2$ change from baseline run during perturbation-based spatial sensitivity analysis (Section 2.5). (b) Most dominant process-based predictor variable mapped by largest absolute mean $p\text{CO}_2$ change from baseline run during perturbation-based spatial sensitivity analysis (excluding top three variables from (a)). No grid cells displayed Chl or Chl anomaly as the largest absolute mean $p\text{CO}_2$ change from baseline over the full study time range (1998–2019). Major river outflows are labeled for reference.

Nearshore regions experience a range of predictors with prominent features mostly controlled by salinity (SSS and SSS anomaly) in coastal estuarine areas (Figure 7b), and tidally mixed areas (e.g., Juan de Fuca Strait, Johnstone Strait; Figure 4a). In additional regions where freshwater discharge is important (e.g., Table S2 in Supporting Information S1), SSH and SSH anomaly emerge as important predictors potentially linked to discharge associated changes to nearshore sea level (Figure 7b; Durand et al., 2019). In the nearshore Gulf of Alaska, SSH could also be linked to coastal downwelling strength (Hauri et al., 2024). Neither perturbation to Chl nor Chl anomaly resulted in the largest absolute mean $p\text{CO}_2$ change from baseline over 264 months in a single grid cell (Figure 7b). However, seasonally Chl emerges as a prominent predictor in scattered grid cells along nearshore West Coast Vancouver Island and in the Southeast Alaska Archipelago during the spring (i.e., March, April, and May; not shown).

5.4. Air-Sea $p\text{CO}_2$ Trends

Trends in the last decades (1998–2019) in $\Delta p\text{CO}_2$ (sea-air) display spatial heterogeneity in the coastal Northeast Pacific, with a gradient of smaller trends moving offshore. A linear fit was applied to the $\Delta p\text{CO}_2$ anomaly time

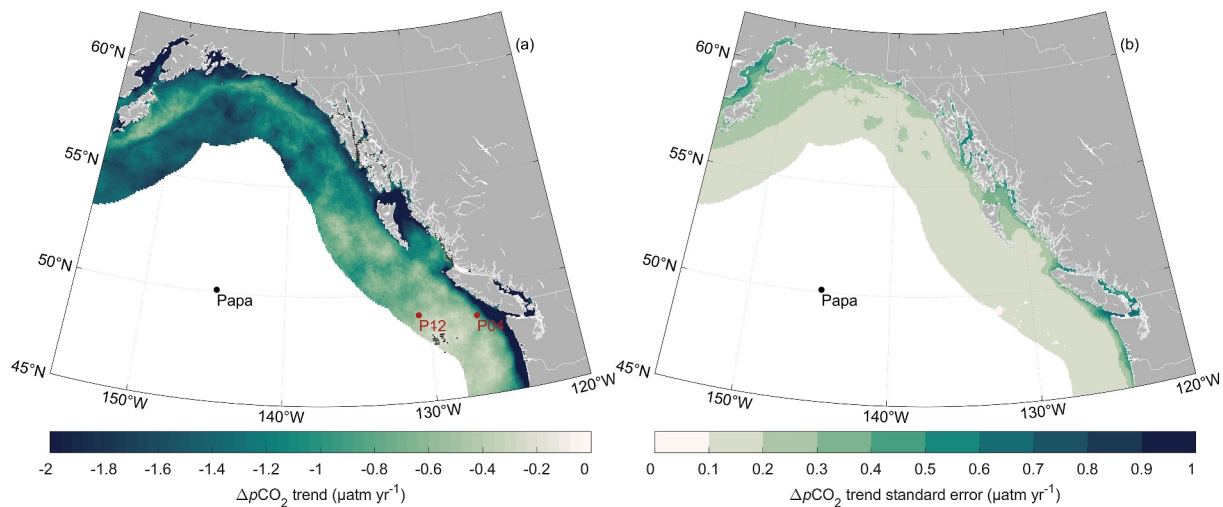


Figure 8. 1998–2019 trend in (a) $\Delta p\text{CO}_2$ anomaly (i.e., deseasonalized) where more negative (darker) values indicate an increase in air-sea $p\text{CO}_2$ disequilibria with time. Black crosshatches show grid cells with an insignificant calculated trend (outside the 95% confidence level; $p \geq 0.05$; 0.4% of total grid cells). (b) Standard error of the estimated slope in the $\Delta p\text{CO}_2$ trend fit.

series within each grid cell to calculate the trend and standard error (i.e., deseasonalized; Section 2.2). Regions that experience an increase in surface ocean $p\text{CO}_2$ close to the increase in atmospheric (i.e., resulting in a small $\Delta p\text{CO}_2$ trend) are spatially distinct from those that have an insignificant trend in $p\text{CO}_2$ leading to a large divergence with the atmosphere (i.e., large $\Delta p\text{CO}_2$ trend). Grid cells with a small $\Delta p\text{CO}_2$ trend are dominantly located in the outer coast (>50 km offshore) and in the southeast of the study area (Figure 8a). Trends are closer to the atmospheric trend in this region ($2.12 \mu\text{atm yr}^{-1}$), meaning any change in the carbon sink due to anthropogenic climate change will require long observation time series to detect, as the signal is small relative to internal variability (Gooya et al., 2023; McKinley et al., 2016; Resplandy et al., 2015; Sutton et al., 2019). We report trends in $p\text{CO}_2$ that are similar to those observed at time series sites along Fisheries and Ocean Canada Line P stations (this study: $P4 = 1.3 \pm 0.1 \mu\text{atm yr}^{-1}$; $P12 = 1.6 \pm 0.1 \mu\text{atm yr}^{-1}$; comparable to Franco et al. (2021): $P4 = 1.0 \pm 1.4 \mu\text{atm yr}^{-1}$; $P12 = 1.5 \pm 0.6 \mu\text{atm yr}^{-1}$).

Large $\Delta p\text{CO}_2$ trends (and low or insignificant $p\text{CO}_2$ trends) occur in regions experiencing strong connectivity to the older subsurface waters of the Northeast Pacific (e.g., subpolar Alaskan Gyre, west coast upwelling zone; Figure 8a). This older water has a lower anthropogenic carbon load (Carter et al., 2019; Clement & Gruber, 2018; Gruber et al., 2019; Sabine et al., 2004), which may be responsible for the lag in the increase in surface ocean $p\text{CO}_2$ (e.g., Duke et al., 2023b). The $\Delta p\text{CO}_2$ trend in the Alaska Gyre is dominated by the winter trend, whereas the west coast upwelling zone is dominated by the summer trend (Figure S14 in Supporting Information S1). These seasonal trends coincide with the timing of greatest connectivity to depth in each region. Strongest Alaskan gyre upwelling occurs in winter (Gargett, 1991; Talley, 1985), whereas the coastal upwelling season is spring and summer (Dorman & Winant, 1995; Hsieh et al., 1995) with downwelling occurring in the winter (Section 5.1; Thomson & Ware, 1996). In the nearshore (e.g., Southeast Alaska Archipelago, Salish Sea), subsurface waters exchange through estuarine flow and tidal mixing. In these regions, we report low or insignificant winter $\Delta p\text{CO}_2$ trends and large negative summer trends in agreement with regional model results (e.g., Jarníková, Ianson, et al., 2022). Increasing summer air-sea $p\text{CO}_2$ disequilibria enhances ocean CO_2 uptake, whereas winter air-sea disequilibria has remained relatively constant, maintaining ocean outgassing. In winter, light limits biological productivity, resulting in higher total CO_2 in the surface (Evans et al., 2019; Ianson et al., 2016; Simpson et al., 2022). This increase in total CO_2 reduces the buffer capacity of the carbonate system (Revelle & Suess, 1957), so that the $p\text{CO}_2$ increase due to anthropogenic carbon uptake is larger than it is in summer in many temperate zones (e.g., Jarníková, Ianson, et al., 2022; Landschützer et al., 2018). Our findings are consistent with global $\Delta p\text{CO}_2$ trend estimates where most coastal regions appear to exhibit negative $\Delta p\text{CO}_2$ trends likely becoming stronger atmospheric CO_2 sinks or weaker sources (Fennel et al., 2019; Laruelle et al., 2018; Resplandy et al., 2024; Roobaert et al., 2024; Wang et al., 2017). However, the rate of change in the air-sea CO_2 flux can be

amplified or dampened in some regions by changes in wind speed patterns (Griffin et al., 2010; Resplandy et al., 2024; Roobaert et al., 2024).

6. Conclusions

Our high-resolution, neural network created $p\text{CO}_2$ product reproduces observed coastal Northeast Pacific Ocean variability well, from the outer transitional zone to the nearshore (0–25 km offshore). We interpolated sparse observations using non-linear relationships developed with a neural network based on predictor data from satellite and reanalysis products to create a continuous, gridded monthly $p\text{CO}_2$ estimate at a $1/12^\circ$ spatial resolution, inclusive of the nearshore. This $p\text{CO}_2$ product provides a baseline environmental context for $p\text{CO}_2$ and air-sea CO_2 flux variability in the study area with an uncertainty of 50 μatm and $0.2 \text{ mol m}^{-2} \text{ yr}^{-1}$, respectively. The product resolves seasonal variability (phase and amplitude) and broad spatial patterns well compared to high-resolution in situ observations. The product is not designed to capture daily—weekly variability. While high frequency, in situ measurements in SOCAT provide valuable insights for specific process studies and can inform the development and parameterization of mechanistic regional models, they are limited in coverage. The created product here addresses this gap by offering continuous estimates in the study area lacking observations, making it a powerful tool for model evaluation.

A unique ANN sensitivity analysis shows that variations in $p\text{CO}_2$ results agree with mechanistic drivers even though the ANN itself is purely empirical. ANNs are not based on predefined equations but their ability to capture information inherent to the training data, preventing any explicit explanation of how predictor variables and their output are related. We suggest a new systematic sensitivity analysis introducing perturbations to predictor variables, with a consideration for natural spatial variability, to produce mapped variable importance rankings. This approach offers insight providing greater transparency to complex ANN techniques.

We quantify the coastal Northeast Pacific as a net sink for atmospheric CO_2 . The region displays large spatial heterogeneity between outgassing in the nearshore and uptake on the outer coast. Net annual air-sea CO_2 flux is largely anticorrelated with seasonal air-sea CO_2 flux amplitude. Patterns inherent to specific regions drive this anticorrelation, including circulation and opposing seasonal upwelling/relaxation versus downwelling, and may make the relationship regionally specific rather than applicable to the wider global coastal ocean. Our results also emphasize the importance of including nearshore fluxes (often omitted by other coastal products), which are likely to be a source reducing the net coastal sink, when constructing marine carbon budgets (e.g., Legge et al., 2020). These findings could be potentially important considerations for reporting marine carbon dioxide removal approaches in the study area, as interventions impacting source areas are treated differently from those enhancing natural sinks (Verra, 2023).

Trends over the last decades show outer coast $p\text{CO}_2$ may be experiencing the largest increase in air-sea $p\text{CO}_2$ disequilibrium, due to strong connectivity with subsurface waters low in anthropogenic CO_2 , while $p\text{CO}_2$ in the North Pacific Current region tracks increasing atmospheric $p\text{CO}_2$ more closely. Trends reported here across the coastal Northeast Pacific indicate most regions are likely to become stronger atmospheric CO_2 sinks or weaker sources.

Improving regional observational coverage and continuity and advancing the ANN approach will improve future air-sea CO_2 flux estimates. Some regions in the coastal Gulf of Alaska display large net annual air-sea CO_2 fluxes (e.g., Cook Inlet) yet are extremely sparsely monitored. A higher temporal resolution, such as daily, could enable the ANN to capture highly episodic air-sea CO_2 flux events common to the nearshore. However, this approach would dramatically reduce the percent coverage of observation training targets. A solution may be creating ANN non-linear relationships to interpolate $p\text{CO}_2$ directly from in situ observations. Using high frequency, collocated sensors and non-uniform “highest available resolution” satellite and reanalysis data sets for predictor variables not collected in situ, a higher temporal and/or spatial resolution coastal product could be developed without substantial loss in ANN training targets.

Conflict of Interest

The authors declare no conflicts of interest relevant to this study.

Data Availability Statement

All data used is publicly available. ANN-NEPc $p\text{CO}_2$ and air-sea CO_2 flux fields created for this publication are available through the National Center for Environmental Information (NCEI Accession 0290365; Duke et al., 2024). $p\text{CO}_2$ data are from the Surface Ocean CO_2 Atlas (SOCAT) v2021 (available at <https://www.socat.info/>; Bakker et al., 2016) as well as additional data from the Fisheries and Oceans Canada February 2019 Line P cruise, a West Coast Ocean Acidification cruise from July and August 2010 (Evans et al., 2012), and La Perouse cruises from May 2007 and May 2010 (available at <https://www.waterproperties.ca/linep/>). Sea surface temperature and chlorophyll-a are from the European Space Agency Climate Change Initiative (available at <https://climate.esa.int/en/odp/#/dashboard>; Good et al., 2019; Sathyendranath et al., 2021). Sea surface salinity and SSH are from Copernicus Marine Environment Monitoring Service (E.U. Copernicus Marine Service Information (CMEMS), 2020). Ocean surface wind data at 10 m height are from Regional Deterministic Reforecast System (available at <https://caspar-data.ca/caspar>; detailed here <https://github.com/julemai/CaSPAR>; Mai et al., 2020). Atmospheric $p\text{CO}_2$ values are from Jersild et al. (2017) (NCEI Accession 0160558), version v2020. A description of the calculation from $\chi\text{CO}_{2,\text{atm_dry}}$ to $p\text{CO}_{2,\text{atm_wet}}$ are presented in Landschützer et al. (2013). Mooring data used in analysis are also available through the National Center for Environmental Information (NOAA moorings: NCEI Accession 0173932; Sutton et al., 2018); and Hakai Institute Quadra Island Field Station: (NCEI Accession 0208638; Evans et al., 2020).

Acknowledgments

Funding for this project was provided by the Natural Sciences and Engineering Research Council of Canada (NSERC) through the Advancing Climate Change Science in Canada program (Grant ACCPJ 536173-18) to RH. Funding from Fisheries and Oceans Canada's Aquatic Climate Change Adaptation Service Program to DI supported the analysis of recent underway $p\text{CO}_2$ measurements made by the Line-P program (Grant 96036). PD financial support also provided by a Natural Sciences and Engineering Research Council of Canada (NSERC) Doctoral Postgraduate Scholarship and the joint Fisheries and Oceans Canada (DFO) and National Oceanic and Atmospheric Administration (NOAA) Ocean Acidification Collaborative Funding Initiative. Fisheries and Oceans Canada (DFO) runs the Line P monitoring program. National Oceanic and Atmospheric Administration (NOAA) operates the Kodiak, Gulf of Alaska Ocean Acidification, Chá bá, and Cape Elizabeth moorings. Hakai Institute operates Quadra Island Station. We extend our thanks to Jamie Shutter and Dan Ford for their valuable brainstorming efforts regarding the $p\text{CO}_2$ temperature correction section. We are grateful to Wiley Evans for sharing previously published $p\text{CO}_2$ data from the 2010 West Coast Ocean Acidification cruise. We also want to thank Philippe Tortell and Robert Izett for providing previously published $p\text{CO}_2$ data from the May 2007 and May 2010 La Perouse cruises.

References

- Asher, E., Dacey, J. W., Ianson, D., Peña, A., & Tortell, P. D. (2017). Concentrations and cycling of DMS, DMSP, and DMSO in coastal and offshore waters of the Subarctic Pacific during summer, 2010-2011. *Journal of Geophysical Research: Oceans*, 122(4), 2647–2651. <https://doi.org/10.1002/2016JC012465>. Received
- Atamanchuk, D., Koelling, J., Send, U., & Wallace, D. W. R. (2020). Rapid transfer of oxygen to the deep ocean mediated by bubbles. *Nature Geoscience*, 13(3), 232–237. <https://doi.org/10.1038/s41561-020-0532-2>
- Bakker, D. C. E., Pfeil, B., Landa, C. S., Metzl, N., O'Brien, K. M., Olsen, A., et al. (2016). A multi-decade record of high-quality $f\text{CO}_2$ data in version 3 of the Surface Ocean CO_2 Atlas (SOCAT). *Earth System Science Data*, 8(2), 383–413. <https://doi.org/10.5194/essd-8-383-2016>
- Batten, S. D., & Crawford, W. R. (2005). The influence of coastal origin eddies on oceanic plankton distributions in the eastern Gulf of Alaska. *Deep-Sea Research Part II Topical Studies in Oceanography*, 52(7–8), 991–1009. <https://doi.org/10.1016/j.dsr2.2005.02.009>
- Bauer, J. E., Cai, W.-J., Raymond, P. A., Bianchi, T. S., Hopkinson, C. S., & Regnier, P. A. G. (2013). The changing carbon cycle of the coastal ocean. *Nature*, 504(7478), 61–70. <https://doi.org/10.1038/nature12857>
- Benway, H., Alin, S., Boyer, E., Cai, W. J., Coble, P., Cross, J., et al. (2016). A science plan for carbon cycle research in north American coastal waters. Report of the coastal CARbon synthesis (CCARS) community workshop, August 19-21, 2014. In *Ocean carbon and biogeochemistry program and North American carbon program*. <https://doi.org/10.1575/1912/7777>
- Bourgeois, T., Orr, J. C., Resplandy, L., Terhaar, J., Ethé, C., Gehlen, M., & Bopp, L. (2016). Coastal-ocean uptake of anthropogenic carbon. *Biogeosciences*, 13(14), 4167–4185. <https://doi.org/10.5194/bg-13-4167-2016>
- Broullón, D., Pérez, F. F., Velo, A., Hoppema, M., Olsen, A., Takahashi, T., et al. (2018). A global monthly climatology of total alkalinity: A neural network approach. *Earth System Science Data Discussions*, 2013(August 2019), 1–31. <https://doi.org/10.5194/essd-2018-111>
- Carter, B. R., Feely, R. A., Wanninkhof, R., Kouketsu, S., Sonnerup, R. E., Pardo, P. C., et al. (2019). Pacific anthropogenic carbon between 1991 and 2017. *Global Biogeochemical Cycles*, 33(5), 597–617. <https://doi.org/10.1029/2018GB006154>
- Chan, F., Barth, J. A., Blanchette, C. A., Byrne, R. H., Chavez, F., Cheriton, O., et al. (2017). Persistent spatial structuring of coastal ocean acidification in the California Current System. *Scientific Reports*, 7(1), 1–7. <https://doi.org/10.1038/s41598-017-02777-y>
- Chau, T. T. T., Gehlen, M., & Chevallier, F. (2022). A seamless ensemble-based reconstruction of surface ocean $p\text{CO}_2$ and air-sea CO_2 fluxes over the global coastal and open oceans. *Biogeosciences*, 19(4), 1087–1109. <https://doi.org/10.5194/bg-19-1087-2022>
- Chavez, F. P., Takahashi, T., Cai, W. J., Friederich, G., Hales, B., Wanninkhof, R., & Feely, R. A. (2007). Coastal oceans. In *The first state of the carbon cycle report (SOCCR): The north American carbon budget and implications for the global carbon cycle* (pp. 157–166). US Climate Change Science Program.
- Chen, C., & Borges, A. V. (2009). Reconciling opposing views on carbon cycling in the coastal ocean: Continental shelves as sinks and near-shore ecosystems as sources of atmospheric CO_2 . *Deep-Sea Research Part II Topical Studies in Oceanography*, 56(8–10), 578–590. <https://doi.org/10.1016/j.dsr2.2008.12.009>
- Chen, S., Hu, C., Byrne, R. H., Robbins, L. L., & Yang, B. (2016). Remote estimation of surface $p\text{CO}_2$ on the West Florida Shelf. *Continental Shelf Research*, 128(December 2015), 10–25. <https://doi.org/10.1016/j.csr.2016.09.004>
- Christensen, J. P. (1994). Carbon export from continental shelves, denitrification and atmospheric carbon dioxide. *Continental Shelf Research*, 14(5), 547–576. [https://doi.org/10.1016/0278-4343\(94\)90103-1](https://doi.org/10.1016/0278-4343(94)90103-1)
- Clement, D., & Gruber, N. (2018). The eMLR (C*) method to determine decadal changes in the global ocean storage of anthropogenic CO_2 (pp. 654–679). <https://doi.org/10.1002/2017GB005819>
- Coyle, K. O., Cheng, W., Hinckley, S. L., Lessard, E. J., Whittedge, T., Hermann, A. J., & Hedstrom, K. (2012). Model and field observations of effects of circulation on the timing and magnitude of nitrate utilization and production on the northern Gulf of Alaska shelf. *Progress in Oceanography*, 103, 16–41. <https://doi.org/10.1016/j.pocean.2012.03.002>
- Crawford, W. R., Brickley, P. J., & Thomas, A. C. (2007). Mesoscale eddies dominate surface phytoplankton in northern Gulf of Alaska. *Progress in Oceanography*, 75(2), 287–303. <https://doi.org/10.1016/j.pocean.2007.08.016>
- Crawford, W. R., & Whitney, F. A. (1999). Mesoscale eddy swirl with data in Gulf of Alaska. *Eos*, 80(33), 365–370. <https://doi.org/10.1029/EO080i033p00365-01>
- Dai, M. (2021). What are the exchanges of carbon between the land-ocean-ice continuum? In R. Wanninkhof, C. Sabine, & S. Aricò (Eds.) *Integrated ocean carbon research: A summary of ocean carbon research, and vision of coordinated ocean carbon research and observations*

for the next decade (p. 20). Intergovernmental Oceanographic Commission. Retrieved from <https://unesdoc.unesco.org/ark:/48223/pf0000376708.locale=en>

- Dai, M., Su, J., Zhao, Y., Hofmann, E. E., Cao, Z., Cai, W., et al. (2022). Carbon fluxes in the Coastal Ocean: Synthesis, boundary processes, and future trends. *Annual Review of Earth and Planetary Sciences*, 50(1), 593–626. <https://doi.org/10.1146/annurev-earth-032320-090746>
- de Oña, J., & Garrido, C. (2014). Extracting the contribution of independent variables in neural network models: A new approach to handle instability. *Neural Computing & Applications*, 25(3–4), 859–869. <https://doi.org/10.1007/s00521-014-1573-5>
- Dorman, C. E., & Winant, C. D. (1995). Buoy observations of the atmosphere along the west coast of the United States, 1981–1990. *Journal of Geophysical Research*, 100(C8), 16029–16044. <https://doi.org/10.1029/95jc00964>
- Duke, P. J., Hamme, R. C., Ianson, D., Landschützer, P., Ahmed, M. M. M., Swart, N. C., & Covert, P. A. (2023a). ANN-NEP: A monthly surface pCO₂ product for the Northeast Pacific open ocean from 1998-01-01 to 2019-12-31 (NCEI accession 0277836). gov.noaa.nodc:0277836 [Dataset]. NOAA National Centers for Environmental Information. <https://doi.org/10.25921/c1w8-6v02>
- Duke, P. J., Hamme, R. C., Ianson, D., Landschützer, P., Ahmed, M. M. M., Swart, N. C., & Covert, P. A. (2023b). Estimating marine carbon uptake in the northeast Pacific using a neural network approach. *Biogeosciences*, 20(18), 3919–3941. <https://doi.org/10.5194/bg-20-3919-2023>
- Duke, P. J., Hamme, R. C., Ianson, D., Landschützer, P., Swart, N. C., & Covert, P. A. (2024). ANN-NEPc: A monthly surface pCO₂ product for the Northeast Pacific coastal ocean from 1998-01-01 to 2019-12-31 [Dataset]. NOAA National Centers for Environmental Information (NCEI). <https://doi.org/10.25921/4jvk-y051>
- Duke, P. J., Richaud, B., Arruda, R., Länger, J., Schuler, K., Gooya, P., et al. (2023). Canada's marine carbon sink: An early career perspective on the state of research and existing knowledge gaps. *Facets*, 8, 1–21. <https://doi.org/10.1139/facets-2022-0214>
- Durand, F., Picuch, C. G., Becker, M., Papa, F., Raju, S. V., Khan, J. U., & Ponte, R. M. (2019). Impact of continental freshwater runoff on coastal sea level. *Surveys in Geophysics*, 40(6), 1437–1466. <https://doi.org/10.1007/s10712-019-09536-w>
- E.U. Copernicus Marine Service Information (CMEMS). (2020). Global Ocean physics reanalysis [Dataset]. *Marine Data Store (MDS)*. <https://doi.org/10.48670/moi-00021>
- Evans, W., Hales, B., & Strutton, P. G. (2011). Seasonal cycle of surface ocean pCO₂ on the Oregon shelf. *Journal of Geophysical Research*, 116(C5), C05012. <https://doi.org/10.1029/2010JC006625>
- Evans, W., Hales, B., Strutton, P. G., & Ianson, D. (2012). Sea-air CO₂ fluxes in the western Canadian coastal ocean. *Progress in Oceanography*, 101(1), 78–91. <https://doi.org/10.1016/j.poccean.2012.01.003>
- Evans, W., Hales, B., Strutton, P. G., Shearman, R. K., & Barth, J. A. (2015). Failure to bloom: Intense upwelling results in negligible phytoplankton response and prolonged CO₂ outgassing over the Oregon shelf. *Journal of Geophysical Research: Oceans*, 120(3), 1446–1461. <https://doi.org/10.1002/2014JC010580>
- Evans, W., Lebon, G. T., Harrington, C. D., Takeshita, Y., Bidlack, A., & Bay, H. (2022). Marine CO₂ system variability along the northeast Pacific inside Passage determined from an Alaskan ferry. *Biogeosciences*, 19(4), 1277–1301. <https://doi.org/10.5194/bg-19-1277-2022>
- Evans, W., & Mathis, J. T. (2013). The Gulf of Alaska coastal ocean as an atmospheric CO₂ sink. *Continental Shelf Research*, 65, 52–63. <https://doi.org/10.1016/j.csr.2013.06.013>
- Evans, W., Pocock, K., Hare, A., Weekes, C., Hales, B., Jackson, J., et al. (2019). Marine CO₂ patterns in the northern Salish Sea. *Frontiers in Marine Science*, 5(JAN), 1–18. <https://doi.org/10.3389/fmars.2018.00536>
- Evans, W., Pocock, K., Weekes, C., & Hare, A. (2020). High-resolution record of surface seawater carbon dioxide (CO₂) content collected from Hakai Institute Quadra Island field station in hyacinthe Bay, British Columbia, Canada from 2014-12-19 to 2023-12-19 [Dataset]. NOAA National Centers for Environmental Information. <https://doi.org/10.25921/v5j2-x847>
- Fassbender, A. J., Alin, S. R., Feely, R. A., Sutton, A. J., Newton, J. A., Krembs, C., et al. (2018). Seasonal carbonate chemistry variability in marine surface waters of the US Pacific Northwest. *Earth System Science Data*, 10(3), 1367–1401. <https://doi.org/10.5194/essd-10-1367-2018>
- Feely, R. A., Sabine, C. L., Hernandez-Ayon, J. M., Ianson, D., & Hales, B. (2008). Evidence for upwelling of corrosive “acidified” water onto the continental shelf. *Science*, 320(5882), 1490–1492. <https://doi.org/10.1126/science.1155676>
- Fennel, K., Alin, S., Barbero, L., Evans, W., Bourgeois, T., Cooley, S., et al. (2019). Carbon cycling in the North American Coastal Ocean: A synthesis. *Biogeosciences*, 16(6), 1281–1304. <https://doi.org/10.5194/bg-16-1281-2019>
- Fiechter, J., & Moore, A. M. (2009). Interannual spring bloom variability and Ekman pumping in the coastal Gulf of Alaska. *Journal of Geophysical Research*, 114, C6. <https://doi.org/10.1029/2008JC005140>
- Ford, D. J., Tilstone, G. H., Shutler, J. D., & Kitidis, V. (2022). Derivation of seawater pCO₂ from net community production identifies the South Atlantic Ocean as a CO₂ source. *Biogeosciences*, 19(1), 93–115. <https://doi.org/10.5194/bg-19-93-2022>
- Ford, D. J., Tilstone, G. H., Shutler, J. D., Kitidis, V., Lobanova, P., Schwarz, J., et al. (2021). Wind speed and mesoscale features drive net autotrophy in the South Atlantic Ocean. *Remote Sensing of Environment*, 260(July 2020), 112435. <https://doi.org/10.1016/j.rse.2021.112435>
- Fourrier, M., Coppola, L., Claustre, H., D'Ortenzio, F., Sauzède, R., & Gattuso, J. P. (2020). A regional neural network approach to estimate water-column nutrient concentrations and carbonate system variables in the Mediterranean sea: CANYON-MED. *Frontiers in Marine Science*, 7(August), 1–20. <https://doi.org/10.3389/fmars.2020.00620>
- Franco, A. C., Ianson, D., Ross, T., Hamme, R. C., Monahan, A. H., Christian, J. R., et al. (2021). Anthropogenic and climatic contributions to observed carbon system trends in the Northeast Pacific. *Global Biogeochemical Cycles*, 35(7), 1–21. <https://doi.org/10.1029/2020gb006829>
- Friedlingstein, P., O'Sullivan, M., Jones, M. W., Andrew, R. M., Bakker, D. C. E., Hauck, J., et al. (2023). Global carbon budget 2023. *Earth System Science Data*, 15(12), 5301–5369. <https://doi.org/10.5194/essd-15-5301-2023>
- Gargett, A. E. (1991). Physical processes and the maintenance of nutrient-rich euphotic zones. *Limnology & Oceanography*, 36(8), 1527–1545. <https://doi.org/10.4319/lo.1991.36.8.1527>
- Good, S. A., Embury, O., Bulgin, C. E., & Mittaz, J. (2019). ESA Sea Surface temperature climate change Initiative (SST_cci): Level 4 analysis climate data record, version 2.1 [Dataset]. Centre for Environmental Data Analysis. <https://doi.org/10.5285/62c0f97b1eac4e0197a674870afe1ee6>
- Gooya, P., Swart, N. C., & Hamme, R. C. (2023). Time-varying changes and uncertainties in the CMIP6 ocean carbon sink from global to local scale. *Earth System Dynamics*, 14(2), 383–398. <https://doi.org/10.5194/esd-14-383-2023>
- Griffin, B. J., Kohfeld, K. E., Cooper, A. B., & Boenisch, G. (2010). Importance of location for describing typical and extreme wind speed behavior. *Geophysical Research Letters*, 37(22), L22804. <https://doi.org/10.1029/2010GL045052>
- Gruber, N., Clement, D., Carter, B. R., Feely, R. A., van Heuven, S., Hoppema, M., et al. (2019). The oceanic sink for anthropogenic CO₂ from 1994 to 2007. *Science*, 363(6432), 1193–1199. <https://doi.org/10.1126/science.aau5153>
- Hales, B., Strutton, P. G., Saraceno, M., Letelier, R., Takahashi, T., Feely, R., et al. (2012). Satellite-based prediction of pCO₂ in coastal waters of the eastern North Pacific. *Progress in Oceanography*, 103, 1–15. <https://doi.org/10.1016/j.poccean.2012.03.001>
- Hales, B., Takahashi, T., & Bandstra, L. (2005). Atmospheric CO₂ uptake by a coastal upwelling system. *Global Biogeochemical Cycles*, 19(1), GB1009. <https://doi.org/10.1029/2004GB002295>

- Hauri, C., Pagès, R., Hedstrom, K., Doney, S. C., Dupont, S., Ferriss, B., & Stuecker, M. F. (2024). More than marine heatwaves: A new regime of heat, acidity, and low oxygen compound extreme events in the Gulf of Alaska. *AGU Advances*, 5(1), e2023AV001039. <https://doi.org/10.1029/2023AV001039>
- Hauri, C., Pagès, R., McDonnell, A. M. P., Stuecker, M. F., Danielson, S. L., Hedstrom, K., et al. (2021). Modulation of ocean acidification by decadal climate variability in the Gulf of Alaska. *Communications Earth & Environment*, 2(1), 1–7. <https://doi.org/10.1038/s43247-021-00254-z>
- Hauri, C., Schultz, C., Hedstrom, K., Danielson, S., Irving, B., C. Doney, S., et al. (2020). A regional hindcast model simulating ecosystem dynamics, inorganic carbon chemistry, and ocean acidification in the Gulf of Alaska. *Biogeosciences*, 17(14), 3837–3857. <https://doi.org/10.5194/bg-17-3837-2020>
- Hermann, A. J., Hinckley, S., Dobbins, E. L., Haidvogel, D. B., Bond, N. A., Mordy, C., et al. (2009). Quantifying cross-shelf and vertical nutrient flux in the Coastal Gulf of Alaska with a spatially nested, coupled biophysical model. *Deep Sea Research Part II: Topical Studies in Oceanography*, 56(24), 2474–2486. <https://doi.org/10.1016/j.dsr2.2009.02.008>
- Hsieh, W. W., Ware, D. A., & Thomson, R. E. (1995). Wind-induced upwelling along the west coast of North America, 1899–1988. *Canadian Journal of Fisheries and Aquatic Sciences*, 52(2), 325–334. <https://doi.org/10.1139/f95-033>
- Ianson, D., & Allen, S. E. (2002). A two-dimensional nitrogen and carbon flux model in a coastal upwelling region. *Global Biogeochemical Cycles*, 16(1). <https://doi.org/10.1029/2001gb001451>
- Ianson, D., Allen, S. E., Harris, S. L., Orians, K. J., Varela, D. E., & Wong, C. S. (2003). The inorganic carbon system in the coastal upwelling region west of Vancouver Island, Canada. *Deep-Sea Research Part I Oceanographic Research Papers*, 50(8), 1023–1042. [https://doi.org/10.1016/S0967-0637\(03\)00114-6](https://doi.org/10.1016/S0967-0637(03)00114-6)
- Ianson, D., Allen, S. E., Moore-Maley, B. L., Johannessen, S. C., & Macdonald, R. W. (2016). Vulnerability of a semienclosed estuarine sea to ocean acidification in contrast with hypoxia. *Geophysical Research Letters*, 43(11), 5793–5801. <https://doi.org/10.1002/2016GL068996>
- Ianson, D., Feely, R. A., Sabine, C. L., & Juraneck, L. W. (2009). Features of coastal upwelling regions that determine net air-sea CO₂ flux. *Journal of Oceanography*, 65(5), 677–687. <https://doi.org/10.1007/s10872-009-0059-z>
- Jarňíková, T., Ianson, D., Allen, S. E., Shao, A., & Olson, E. M. (2022). Anthropogenic carbon increase has caused critical shifts in aragonite saturation across a sensitive coastal system. *Global Biogeochemical Cycles*, 36(7). <https://doi.org/10.1029/2021GB007024>
- Jarňíková, T., Olson, E. M., Allen, S. E., Ianson, D., & Suchy, K. D. (2022). A clustering approach to determine biophysical provinces and physical drivers of productivity dynamics in a complex coastal sea. *Ocean Science*, 18(5), 1451–1475. <https://doi.org/10.5194/os-18-1451-2022>
- Jersild, A., Landschützer, P., Gruber, N., & Bakker, D. C. E. (2017). An observation-based global monthly gridded sea surface pCO₂ and air-sea CO₂ flux product from 1982 onward and its monthly climatology (NCEI Accession 0160558) [Dataset]. *NOAA National Centers for Environmental Information*. <https://doi.org/10.7289/v5z899n6>
- Jones, S. D., Le Quéré, C., & Rdenbeck, C. (2012). Autocorrelation characteristics of surface ocean pCO₂ and air-sea CO₂ fluxes. *Global Biogeochemical Cycles*, 26(2), 1–12. <https://doi.org/10.1029/2010GB004017>
- Körtzinger, A. (1999). Determination of carbon dioxide partial pressure (pCO₂). In *Methods of seawater analysis* (pp. 149–158). Verlag Chemie.
- Landschützer, P., Gruber, N., Bakker, D. C. E., & Schuster, U. (2014). Recent variability of the global ocean carbon sink. *Global Biogeochemical Cycles*, 28(9), 927–949. <https://doi.org/10.1002/2014GB004853>
- Landschützer, P., Gruber, N., Bakker, D. C. E., Schuster, U., Nakaoka, S., Payne, M. R., et al. (2013). A neural network-based estimate of the seasonal to inter-annual variability of the Atlantic Ocean carbon sink. *Biogeosciences*, 10(11), 7793–7815. <https://doi.org/10.5194/bg-10-7793-2013>
- Landschützer, P., Gruber, N., Bakker, D. C. E., Stemmler, I., & Six, K. D. (2018). Strengthening seasonal marine CO₂ variations due to increasing atmospheric CO₂. *Nature Climate Change*, 8(2), 146–150. <https://doi.org/10.1038/s41558-017-0057-x>
- Landschützer, P., Laruelle, G. G., Roobaert, A., & Regnier, P. (2020). A uniform pCO₂ climatology combining open and coastal oceans. *Earth System Science Data*, 12(4), 2537–2553. <https://doi.org/10.5194/essd-12-2537-2020>
- Laruelle, G. G., Cai, W.-J., Hu, X., Gruber, N., Mackenzie, F. T., & Regnier, P. (2018). Continental shelves as a variable but increasing global sink for atmospheric carbon dioxide. *Nature Communications*, 9(454), 1–11. <https://doi.org/10.1038/s41467-017-02738-z>
- Laruelle, G. G., Landschützer, P., Gruber, N., Tison, J.-L., Delille, B., & Regnier, P. (2017). Global high-resolution monthly pCO₂ climatology for the coastal ocean derived from neural network interpolation. *Biogeosciences Discussions*, 14(19), 1–40. <https://doi.org/10.5194/bg-2017-64>
- Laruelle, G. G., Lauerwald, R., Pfeil, B., & Regnier, P. (2014). Regionalized global budget of the CO₂ exchange at the air-water interface in continental shelf seas. *Global Biogeochemical Cycles*, 28(11), 1199–1214. <https://doi.org/10.1002/2014GB004832>. Received
- Legge, O., Johnson, M., Hicks, N., Jickells, T., Diesing, M., Aldridge, J., et al. (2020). Carbon on the Northwest European shelf: Contemporary budget and future influences. *Frontiers in Marine Science*, 7(March). <https://doi.org/10.3389/fmars.2020.00143>
- Li, X., Bellerby, R., Ge, J., Wallhead, P., Liu, J., & Yang, A. (2019). Retrieving monthly and interannual total-scale pH on the east China sea shelf using an artificial neural network: ANN-pH-v1. In *Geoscientific model development discussions* (pp. 1–15). <https://doi.org/10.5194/gmd-2019-236>
- Li, X., Bellerby, R. G. J., Wallhead, P., Ge, J., Liu, J., Liu, J., & Yang, A. (2020). A neural network-based analysis of the seasonal variability of surface total alkalinity on the east China sea shelf. *Frontiers in Marine Science*, 7(April), 219. <https://doi.org/10.3389/fmars.2020.00219>
- Linares-Rodríguez, A., Ruiz-Arias, J. A., Pozo-Vazquez, D., & Tovar-Pescador, J. (2013). An artificial neural network ensemble model for estimating global solar radiation from Meteosat satellite images. *Energy*, 61, 636–645. <https://doi.org/10.1016/j.energy.2013.09.008>
- Liu, K.-K., Atkinson, L., Quinones, R., & Talaue-McManus, L. (2010). Carbon and nutrient fluxes in continental margins. In *Global change—The IGBP series*. Springer-Verlag.
- Mackenzie, F. T., Lerman, A., & Ver, L. M. B. (1998). Role of the continental margin in the global carbon balance during the past three centuries. *Geology*, 26(5), 423–426. [https://doi.org/10.1130/0091-7613\(1998\)026<0423:ROTCMI>2.3.CO;2](https://doi.org/10.1130/0091-7613(1998)026<0423:ROTCMI>2.3.CO;2)
- Mai, J., Kornelsen, K. C., Tolson, B. A., Fortin, V., Gasset, N., Bouhemhem, D., et al. (2020). The Canadian surface prediction archive (CaSPAR): A platform to enhance environmental modeling in Canada and globally. *Bulletin of the American Meteorological Society*, 101(3), E341–E356. <https://doi.org/10.1175/BAMS-D-19-0143.1>
- Marchese, C., Hunt, B. P. V., Giannini, F., Ehrler, M., & Costa, M. (2022). Bioregionalization of the coastal and open oceans of British Columbia and Southeast Alaska based on Sentinel-3A satellite-derived phytoplankton seasonality. *Frontiers in Marine Science*, 9(September), 1–22. <https://doi.org/10.3389/fmars.2022.968470>
- McKinley, G. A., Pilcher, D. J., Fay, A. R., Lindsay, K., Long, M. C., & Lovenduski, N. S. (2016). Timescales for detection of trends in the ocean carbon sink. *Nature*, 530(7591), 469–472. <https://doi.org/10.1038/nature16958>
- Messié, M., & Chavez, F. P. (2015). Seasonal regulation of primary production in eastern boundary upwelling systems. *Progress in Oceanography*, 134, 1–18. <https://doi.org/10.1016/j.pocean.2014.10.011>

- Murphy, P. P., Nojiri, Y., Harrison, D. E., & Larkin, N. K. (2001). Scales of spatial variability for surface ocean $p\text{CO}_2$ in the Gulf of Alaska and Bering Sea: Toward a sampling strategy. *Geophysical Research Letters*, 28(6), 1047–1050. <https://doi.org/10.1029/2000GL012375>
- Nemcek, N., Ianson, D., & Tortell, P. D. (2008). A high-resolution survey of DMS, CO_2 , and O_2/Ar distributions in productive coastal waters. *Global Biogeochemical Cycles*, 22(2), 1–13. <https://doi.org/10.1029/2006GB002879>
- Palter, J. B., Nickford, S., & Mu, L. (2023). Ocean carbon dioxide uptake in the tailpipe of industrialized continents. *Geophysical Research Letters*, 50(21), e2023GL104822. <https://doi.org/10.1029/2023GL104822>
- Parard, G., Charantonis, A. A., & Rutgerson, A. (2015). Remote sensing of the sea surface CO_2 of the Baltic Sea using the SOMLO methodology. *Biogeosciences*, 12(11), 3369–3384. <https://doi.org/10.5194/bg-12-3369-2015>
- Parard, G., Charantonis, A. A., & Rutgerson, A. (2016). Using satellite data to estimate partial pressure of CO_2 in the Baltic Sea. *Journal of Geophysical Research G: Biogeosciences*, 121(3), 1002–1015. <https://doi.org/10.1002/2015JG003064>
- Pilcher, D. J., Siedlecki, S. A., Hermann, A. J., Coyle, K. O., Mathis, J. T., & Evans, W. (2018). Simulated impact of glacial runoff on CO_2 uptake in the Gulf of Alaska. *Geophysical Research Letters*, 45(2), 880–890. <https://doi.org/10.1002/2017GL075910>
- Reed, R. K., & Schumacher, J. D. (1986). Current measurements along the shelf break in the Gulf of Alaska. *Journal of Physical Oceanography*, 16(11), 1985–1990. [https://doi.org/10.1175/1520-0485\(1986\)016<1985:CMATSB>2.0.CO;2](https://doi.org/10.1175/1520-0485(1986)016<1985:CMATSB>2.0.CO;2)
- Regnier, P., Resplandy, L., Najjar, R. G., & Ciais, P. (2022). The land-to-ocean loops of the global carbon cycle. *Nature*, 603(7901), 401–410. <https://doi.org/10.1038/s41586-021-04339-9>
- Resplandy, L., Hogikyan, A., Müller, J. D., Najjar, R. G., Bange, H. W., Bianchi, D., et al. (2024). A synthesis of global Coastal Ocean greenhouse gas fluxes. *Global Biogeochemical Cycles*, 38(1), e2023GB007803. <https://doi.org/10.1029/2023GB007803>
- Resplandy, L., Séférian, R., & Bopp, L. (2015). Natural variability of CO_2 and O_2 fluxes: What can we learn from centuries-long climate models simulations? *Journal of Geophysical Research: Oceans*, 120(1), 384–404. <https://doi.org/10.1002/2014JC010463>
- Revelle, R., & Suess, H. E. (1957). Carbon dioxide exchange between atmosphere and Ocean and the question of an increase of atmospheric CO_2 during the past decades. *Tellus*, 9(1), 18–27. <https://doi.org/10.3402/tellusa.v9i1.9075>
- Ribalet, F., Marchetti, A., Hubbard, K. A., Brown, K., Durkin, C. A., Morales, R., et al. (2010). Unveiling a phytoplankton hotspot at a narrow boundary between coastal and offshore waters. *Proceedings of the National Academy of Sciences of the United States of America*, 107(38), 16571–16576. <https://doi.org/10.1073/pnas.1005638107>
- Roobaert, A., Laruelle, G. G., Landschützer, P., Gruber, N., Chou, L., & Regnier, P. (2019). The spatiotemporal dynamics of the sources and sinks of CO_2 in the global Coastal Ocean. *Global Biogeochemical Cycles*, 33(12), 1693–1714. <https://doi.org/10.1029/2019GB006239>
- Roobaert, A., Laruelle, G. G., Landschützer, P., & Regnier, P. (2018). Uncertainty in the global oceanic CO_2 uptake induced by wind forcing: Quantification and spatial analysis. *Biogeosciences*, 15(6), 1701–1720. <https://doi.org/10.5194/bg-15-1701-2018>
- Roobaert, A., Regnier, P., Landschützer, P., & Laruelle, G. G. (2024). A novel sea surface $p\text{CO}_2$ -product for the global coastal ocean resolving trends over 1982–2020. *Earth System Science Data*, 16(1), 421–441. <https://doi.org/10.5194/essd-16-421-2024>
- Sabine, C. L., Feely, R. A., Gruber, N., Key, R. M., Lee, K., Bullister, J. L., et al. (2004). The oceanic sink for anthropogenic CO_2 . *Science*, 305(July), 367–372. <https://doi.org/10.1126/science.1097403>
- Sathyendranath, S., Jackson, T., Brockmann, C., Brotas, V., Calton, B., Chuprin, A., et al. (2021). ESA ocean colour climate change initiative (Ocean_Colour_cci): Global chlorophyll-a data products gridded on a geographic projection, version 5.0 [Dataset]. *Centre for Environmental Data Analysis*. <https://doi.org/10.5285/1d8e7a109e0244aad713e078fd3059a>
- Sharkey, A. J. C. (1999). *Combining artificial neural nets: Ensemble and modular multi-net systems*. Springer.
- Sharp, J. D., Fassbender, A. J., Carter, B. R., Lavin, P. D., & Sutton, A. J. (2022). A monthly surface $p\text{CO}_2$ product for the California Current Large Marine Ecosystem. *Earth System Science Data*, 14(4), 2081–2108. <https://doi.org/10.5194/essd-14-2081-2022>
- Siedlecki, S. A., Pilcher, D. J., Hermann, A. J., Coyle, K., & Mathis, J. (2017). The importance of freshwater to spatial variability of aragonite saturation state in the Gulf of Alaska. *Journal of Geophysical Research: Oceans*, 122(11), 8482–8502. <https://doi.org/10.1002/2017JC012791>
- Simpson, E., Ianson, D., & Kohfeld, K. E. (2022). Using end-member models to estimate seasonal carbonate chemistry and acidification sensitivity in temperate estuaries. *Geophysical Research Letters*, 49(2), e2021GL095579. <https://doi.org/10.1029/2021GL095579>
- Stabeno, P. J., Bond, N. A., Hermann, A. J., Kachel, N. B., Mordy, C. W., & Overland, J. E. (2004). Meteorology and oceanography of the northern Gulf of Alaska. *Continental Shelf Research*, 24(7–8), 859–897. <https://doi.org/10.1016/j.csr.2004.02.007>
- Sun, H., He, J., Chen, Y., & Zhao, B. (2021). Space-time sea surface $p\text{CO}_2$ estimation in the North Atlantic based on CatBoost. *Remote Sensing*, 13(14), 2805. <https://doi.org/10.3390/rs13142805>
- Sutton, A. J., Feely, R. A., Maenner Jones, S., Musielewicz, S., Osborne, J., Dietrich, C., et al. (2018). Autonomous seawater partial pressure of carbon dioxide ($p\text{CO}_2$) and pH time series from 40 surface buoys between 2004 and 2017 [Dataset]. *NOAA National Centers for Environmental Information*. <https://doi.org/10.7289/V5DB8043>
- Sutton, A. J., Feely, R. A., Maenner-Jones, S., Musielwicz, S., Osborne, J., Dietrich, C., et al. (2019). Autonomous seawater $p\text{CO}_2$ and pH time series from 40 surface buoys and the emergence of anthropogenic trends. *Earth System Science Data*, 11(1), 421–439. <https://doi.org/10.5194/essd-11-421-2019>
- Sutton, A. J., Wanninkhof, R., Sabine, C. L., Feely, R. A., Cronin, M. F., & Weller, R. A. (2017). Variability and trends in surface seawater $p\text{CO}_2$ and CO_2 flux in the Pacific Ocean. *Geophysical Research Letters*, 44(11), 5627–5636. <https://doi.org/10.1002/2017GL073814>
- Takahashi, T., Olafsson, J., Goddard, J. G., Chipman, D. W., & Sutherland, S. C. (1993). Seasonal variation of CO_2 and nutrients in the high-latitude surface oceans: A comparative study. *Global Biogeochemical Cycles*, 7(4), 843–878. <https://doi.org/10.1029/93GB02263>
- Takahashi, T., Sutherland, S. C., Feely, R. A., & Wanninkhof, R. (2006). Decadal change of the surface water $p\text{CO}_2$ in the North Pacific: A synthesis of 35 years of observations. *Journal of Geophysical Research*, 111(C7), C07S05. <https://doi.org/10.1029/2005JC003074>
- Takahashi, T., Sutherland, S. C., Sweeney, C., Poisson, A., Metz, N., Tilbrook, B., et al. (2002). Global sea-air CO_2 flux based on climatological surface ocean $p\text{CO}_2$, and seasonal biological and temperature effects. *Deep-Sea Research Part II Topical Studies in Oceanography*, 49(9–10), 1601–1622. [https://doi.org/10.1016/S0967-0645\(02\)00003-6](https://doi.org/10.1016/S0967-0645(02)00003-6)
- Talley, L. D. (1985). Ventilation of the subtropical North Pacific: The shallow salinity minimum. *Journal of Physical Oceanography*, 15(6), 633–649. [https://doi.org/10.1175/1520-0485\(1985\)015<0633:VOTSNP>2.0.CO;2](https://doi.org/10.1175/1520-0485(1985)015<0633:VOTSNP>2.0.CO;2)
- Teeter, L., Hamme, R. C., Ianson, D., & Bianucci, L. (2018). Accurate estimation of net community production from O_2/Ar measurements. *Global Biogeochemical Cycles*, 32(8), 1163–1181. <https://doi.org/10.1029/2017GB005874>
- Thomson, R. E. (1981). Oceanography of the British Columbia coast. In *Canadian special publications of fisheries and aquatic sciences* (Vol. 56).
- Thomson, R. E., & Ware, D. M. (1996). A current velocity index of ocean variability. *Journal of Geophysical Research*, 101(C6), 14297–14310. <https://doi.org/10.1029/96JC01055>
- Tortell, P. D., Merzouk, A., Ianson, D., Pawlowicz, R., & Yelland, D. R. (2012). Influence of regional climate forcing on surface water $p\text{CO}_2$, $\Delta\text{O}_2/\text{Ar}$ and dimethylsulfide (DMS) along the southern British Columbia coast. *Continental Shelf Research*, 47, 119–132. <https://doi.org/10.1016/j.csr.2012.07.007>

- Verra. (2023). *Verified carbon standard program Guide v4.5*. Verra. Retrieved from <https://verra.org/programs/verified-carbon-standard/vcs-version-4-rules-and-requirements/>
- Wang, H., Hu, X., Cai, W.-J., & Sterba-Boatwright, B. (2017). Decadal fCO₂ trends in global ocean margins and adjacent boundary current-influenced areas. *Geophysical Research Letters*, *44*(17), 8962–8970. <https://doi.org/10.1002/2017GL074724>
- Wanninkhof, R. (2014). Relationship between wind speed and gas exchange over the ocean revisited. *Limnology and Oceanography: Methods*, *12*(6), 351–362. <https://doi.org/10.4319/lom.2014.12.351>
- Ward, N. D., Megonigal, J. P., Bond-Lamberty, B., Bailey, V. L., Butman, D., Canuel, E. A., et al. (2020). Representing the function and sensitivity of coastal interfaces in Earth system models. *Nature Communications*, *11*(1), 2458. <https://doi.org/10.1038/s41467-020-16236-2>
- Ware, D. M., & Thomson, R. E. (2005). Bottom-up ecosystem trophic dynamics determine fish production in the Northeast Pacific. *Science*, *308*(5726), 1280–1284. <https://doi.org/10.1126/science.1109049>
- Weingartner, T. J., Coyle, K., Finney, B., Hopcroft, R., Whitlege, T., Brodeur, R., et al. (2002). The Northeast Pacific GLOBEC program: Coastal Gulf of Alaska. *Oceanography*, *15*(2), 48–63. <https://doi.org/10.5670/oceanog.2002.21>
- Weiss, R. F. (1974). Carbon dioxide in water and seawater: The solubility of a non-ideal gas. *Marine Chemistry*, *2*(3), 203–215. [https://doi.org/10.1016/0304-4203\(74\)90015-2](https://doi.org/10.1016/0304-4203(74)90015-2)
- Whitney, F. A., Crawford, W. R., & Harrison, P. J. (2005). Physical processes that enhance nutrient transport and primary productivity in the coastal and open ocean of the subarctic NE Pacific. *Deep-Sea Research Part II Topical Studies in Oceanography*, *52*(5–6), 681–706. <https://doi.org/10.1016/j.dsr2.2004.12.023>
- Whitney, F. A., & Robert, M. (2002). Structure of Haida Eddies and their transport of nutrient from coastal margins into the NE Pacific Ocean. *Journal of Oceanography*, *58*(5), 715–723. <https://doi.org/10.1023/A:1022850508403>
- Wilkerson, F. P., & Dugdale, R. C. (1987). The use of large shipboard barrels and drifters to study the effects of coastal upwelling on phytoplankton dynamics 1, 2. *Limnology & Oceanography*, *32*(2), 368–382. <https://doi.org/10.4319/lo.1987.32.2.0368>
- Wong, C. S., Christian, J. R., Emmy Wong, S. K., Page, J., Xie, L., & Johannessen, S. (2010). Carbon dioxide in surface seawater of the eastern North Pacific ocean (line P), 1973–2005. *Deep-Sea Research Part I Oceanographic Research Papers*, *57*(5), 687–695. <https://doi.org/10.1016/j.dsr.2010.02.003>
- Wu, Z., Wang, H., Liao, E., Hu, C., Edwing, K., Yan, X.-H., & Cai, W.-J. (2024). Air-sea CO₂ flux in the Gulf of Mexico from observations and multiple machine-learning data products. *Progress in Oceanography*, *223*, 103244. <https://doi.org/10.1016/j.poccean.2024.103244>
- Xu, S., Park, K., Wang, Y., Chen, L., Qi, D., & Li, B. (2019). Variations in the summer oceanic pCO₂ and carbon sink in Prydz Bay using the self-organizing map analysis approach. *Biogeosciences*, *16*(3), 797–810. <https://doi.org/10.5194/bg-16-797-2019>

References From the Supporting Information

- Bélair, S., Roch, M., Leduc, A.-M., Vaillancourt, P. A., Laroche, S., & Mailhot, J. (2009). Medium-range quantitative precipitation forecasts from Canada's new 33-km deterministic global operational system. *Weather and Forecasting*, *24*(3), 690–708. <https://doi.org/10.1175/2008WAF2222175.1>
- Côté, J., Gravel, S., Méthot, A., Patoine, A., Roch, M., & Staniforth, A. (1998). The operational CMC-MRB global environmental multiscale (GEM) model. Part I: Design considerations and formulation. *Monthly Weather Review*, *126*(6), 1373–1395. [https://doi.org/10.1175/1520-0493\(1998\)126<1373:TOCMGE>2.0.CO;2](https://doi.org/10.1175/1520-0493(1998)126<1373:TOCMGE>2.0.CO;2)
- Dickson, A. G., Sabine, C. L., & Christian, J. R. (2007). *Guide to best practices for ocean CO₂ measurements* (Vol. 3). PICES Special Publication.
- Dong, Y., Bakker, D. C. E., Bell, T. G., Huang, B., Landschützer, P., Liss, P. S., & Yang, M. (2022). Update on the temperature corrections of global air-sea CO₂ flux estimates. *Global Biogeochemical Cycles*, *36*(9), e2022GB007360. <https://doi.org/10.1029/2022GB007360>
- Gasset, N., Fortin, V., Dimitrijevic, M., Carrera, M., Bilodeau, B., Muncaster, R., et al. (2021). A 10 km North American precipitation and land-surface reanalysis based on the GEM atmospheric model. *Hydrology and Earth System Sciences*, *25*(9), 4917–4945. <https://doi.org/10.5194/hess-25-4917-2021>
- Goddijn-Murphy, L. M., Woolf, D. K., Land, P. E., Shutler, J. D., & Donlon, C. (2015). The OceanFlux Greenhouse Gases methodology for deriving a sea surface climatology of CO₂ fugacity in support of air-sea gas flux studies. *Ocean Science*, *11*(4), 519–541. <https://doi.org/10.5194/os-11-519-2015>
- Jean-Michel, L., Eric, G., Romain, B.-B., Gilles, G., Angélique, M., Marie, D., et al. (2021). The Copernicus global 1/12° oceanic and sea ice GLORYS12 reanalysis. *Frontiers in Earth Science*, *9*(698876), 1–27. <https://doi.org/10.3389/feart.2021.698876>
- Kalnay, E., Kanamitsu, M., Kistler, R., Collins, W., Deaven, D., Gandin, L., et al. (1996). The NCEP/NCAR 40-year reanalysis project. *Bulletin of the American Meteorological Society*, *77*(3), 437–472. [https://doi.org/10.1175/1520-0477\(1996\)077<0437:TNYRP>2.0.CO;2](https://doi.org/10.1175/1520-0477(1996)077<0437:TNYRP>2.0.CO;2)
- Merchant, C. J., Embury, O., Bulgin, C. E., Block, T., Corlett, G. K., Fiedler, E., et al. (2019). Satellite-based time-series of sea-surface temperature since 1981 for climate applications. *Scientific Data*, *6*(1), 1–18. <https://doi.org/10.1038/s41597-019-0236-x>
- O'Carroll, A. G., Armstrong, E. M., Beggs, H. M., Bouali, M., Casey, K. S., Corlett, G. K., et al. (2019). Observational needs of Sea Surface temperature. *Frontiers in Marine Science*, *6*, 420. <https://doi.org/10.3389/fmars.2019.00420>
- Reynolds, R. W., Rayner, N. A., Smith, T. M., Stokes, D. C., & Wang, W. (2002). An improved in situ and satellite SST analysis for climate. *Journal of Climate*, *15*(13), 1609–1625. [https://doi.org/10.1175/1520-0442\(2002\)015<1609:AIISSAS>2.0.CO;2](https://doi.org/10.1175/1520-0442(2002)015<1609:AIISSAS>2.0.CO;2)
- Sarmiento, J. L., & Gruber, N. (2006). *Ocean biogeochemical dynamics*. Princeton University Press.
- Shutler, J. D., Land, P. E., Piolle, J. F., Woolf, D. K., Goddijn-Murphy, L., Paul, F., et al. (2016). FluxEngine: A flexible processing system for calculating atmosphere-ocean carbon dioxide gas fluxes and climatologies. *Journal of Atmospheric and Oceanic Technology*, *33*(4), 741–756. <https://doi.org/10.1175/JTECH-D-14-00204.1>
- Watson, A. J., Schuster, U., Shutler, J. D., Holding, T., Ashton, I. G. C., Landschützer, P., et al. (2020). Revised estimates of ocean-atmosphere CO₂ flux are consistent with ocean carbon inventory. *Nature Communications*, *11*(1), 1–6. <https://doi.org/10.1038/s41467-020-18203-3>
- Woolf, D. K., Land, P. E., Shutler, J. D., Goddijn-Murphy, L. M., & Donlon, C. J. (2016). On the calculation of air-sea fluxes of CO₂ in the presence of temperature and salinity gradients. *Journal of Geophysical Research: Oceans*, *121*(5), 3010–3028. <https://doi.org/10.1002/2015JC011516>
- Yasunaka, S., Siswanto, E., Olsen, A., Hoppema, M., Watanabe, E., Fransson, A., et al. (2018). Arctic Ocean CO₂ uptake: An improved multiyear estimate of the air-sea CO₂ flux incorporating chlorophyll a concentrations. *Biogeosciences*, *15*(6), 1643–1661. <https://doi.org/10.5194/bg-15-1643-2018>